Marine and Petroleum Geology 158 (2023) 106512

Contents lists available at ScienceDirect

Marine and Petroleum Geology

journal homepage: www.elsevier.com/locate/marpetgeo

Gas generation potential and pore characteristics of Jurassic lacustrine shale containing type II kerogen: A case study of the Yabulai Basin, northwestern China

Ruihui Zheng [a,b,c], Chengjin Zhang [b,d], Haizhong Tang [e], Zhihuan Zhang [b,*], Yuan Bao [a], Wenhao Li [f], Leyi Zhao [e], Tao Li [e], Guangli Wang [b]

[a] College of Geology and Environment, Xi'an University of Science and Technology, Xi'an, 710054, PR China
[b] College of Geosciences, China University of Petroleum, Beijing, 102249, PR China
[c] Postdoctoral Research Station of Geological Resources and Geological Engineering, Xi'an University of Science and Technology, Xi'an, 710054, PR China
[d] The First Natural Gas Plant, PetroChina Changqing Oilfield Company, Jingbian, Shaanxi, 718500, PR China
[e] Research Institute of Exploration and Development, PetroChina Yumen Oilfield Company, Jiuquan, Gansu, 735000, PR China
[f] School of Geosciences, China University of Petroleum (East China), Qingdao, 266580, PR China

A R T I C L E I N F O

Keywords:
Type II kerogen
Jurassic lacustrine shale
Gas generation potential
Pore characteristics
Adsorption capacity

A B S T R A C T

Jurassic lacustrine shales containing kerogen types II and III are widely distributed in sedimentary basins around the world. Previous studies on gas generation potential and pore characteristics of Jurassic lacustrine shales mainly focused on type III kerogen, but ignored the systematic study of the shales containing type II kerogen. This led to a poor understanding of the gas generation potential and pore characteristics of Jurassic lacustrine shales, which limits the effective exploration and development of shale gas. Taking the Lower Xinhe (J_2x^1) shale of the Yabulai Basin in northwestern China as the research object, this paper examines the gas generation potential and pore characteristics of a Jurassic lacustrine shale containing type II kerogen. The J_2x^1 shale is largely classified as a very good source rock, kerogen is predominantly type II, with thermal maturity ranging from mature to highly over-mature. The J_2x^1 shale is characterized by low porosity and permeability, and high content of brittle minerals. Different from the Jurassic lacustrine shales containing type III kerogen, the J_2x^1 shales have a large amount of interparticle and intraparticle dissolution pores in the clay minerals as well as organic pores. The porosity and pore structure of the J_2x^1 shale are strongly controlled by total organic carbon (TOC) content. The methane adsorption capacity of the J_2x^1 shale is in the range of 2.10–2.99 m^3/t, which is controlled by TOC content, clay mineral content, temperature and pressure. The geochemical characteristics, mineral composition and adsorption capacity suggest that the J_2x^1 shale has good shale exploration and development potential. A mathematical model is established to describe the various characteristics of methane adsorption capacity with depth and TOC content. The methane adsorption capacity of the J_2x^1 shale first increases and then decreases with increasing depth, with the depth corresponding to the maximum methane adsorption increases with increasing TOC content. When the TOC values of the J_2x^1 shale are mainly between 1% and 10%, the corresponding depth of the maximum methane adsorption capacity is 400–800 m, and the adsorption amount of the shale tends to minimize at a depth range of 2600–5100 m. The favorable shale gas exploration depth of the J_2x^1 shale in the study area increases with increasing TOC content. This research provides a geological reference for the exploration of this Jurassic shale gas in the Yabulai Basin, and the relevant experimental data provide important parameters for the numerical simulation of shale gas reservoirs in the study area. Moreover, the results of this study also provide an important reference for other basins in northwestern China, as well as continental basins with similar geological conditions in other regions.

* Corresponding author.
E-mail address: zhangzh3996@vip.163.com (Z. Zhang).

https://doi.org/10.1016/j.marpetgeo.2023.106512
Received 22 February 2022; Received in revised form 18 September 2023; Accepted 22 September 2023
Available online 24 September 2023

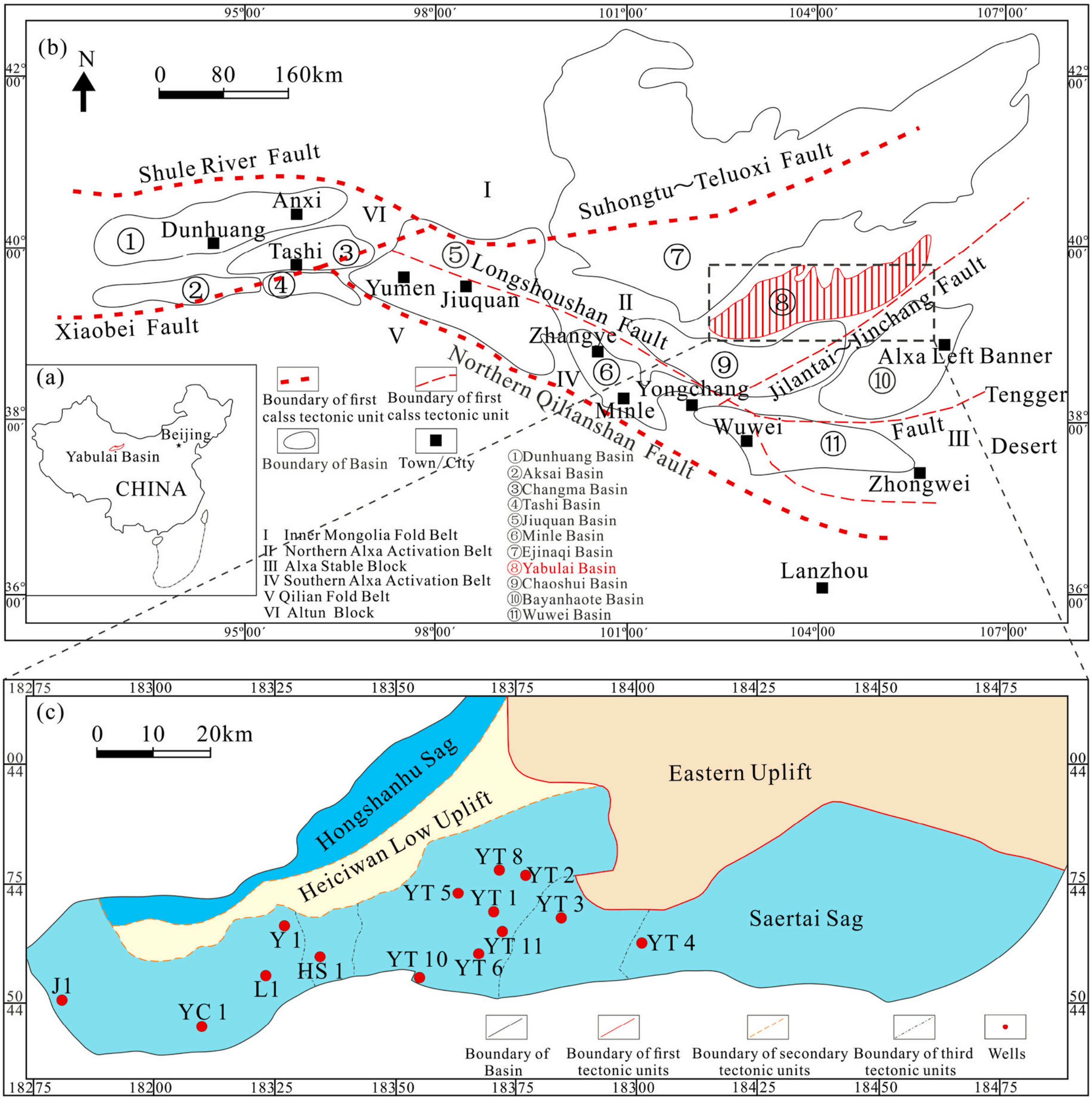

Fig. 1. Location and geological sketch of study areas. (a) Showing the location of the Yabulai Basin in China; (b) Showing the surrounding basins of the Yabulai Basin (modified from Dong, 2014); (c) Structural units and sample collection locations in the Yabulai Basin.

1. Introduction

Large-scale development of shale gas has achieved success in marine shales, such as the Barnett and Longmaxi shales. These shales are dominated by type II organic matter (Jarvie et al., 2007; Jarboe et al., 2015; Li and Horita, 2022). However, as exploration for continental shale gas has not achieved commercial breakthroughs, it is necessary to expand industry's understanding of shale systems. Presently, in China the research on pore characteristics of continental shales have been mainly focused on Triassic shales in the Ordos Basin, Cretaceous shales in the Songliao Basin and Paleogene shales in the Bohai Bay Basin (Liu et al., 2015, 2023; Li et al., 2017). The pore characteristics of Jurassic continental shales were little studied. Continental shales from the Jurassic are widely distributed in sedimentary basins around the world, including larger gas-bearing basins (Ordos, Sichuan, Turpan-Hami, Junggar and West Siberian basins) and smaller gas-bearing basins (Yabulai and Minhe basins) (Chen et al., 1998; Wang et al., 2016; Gao et al., 2018; Han et al., 2020; Burnaz et al., 2022; Li et al., 2023). The sedimentary area of Jurassic continental shale in northwestern China is 127 × 10^4 km^2 (Zhao et al., 1996), with an estimated gas amount of approximately 2.8–5.6 × 10^{12} m^3 (Lu et al., 2009; Dai et al., 2014; Ni et al., 2015), indicating that there exists good shale gas exploration potential in Jurassic continental shales, northwestern China.

Comprehensively evaluating the gas generation potential of organic matter and pore characteristics of shale reservoirs can effectively reduce their exploration risk (Chalmers and Bustin, 2007; Ross and Bustin, 2009; Chen et al., 2019, 2021a; Han et al., 2020; Miao et al., 2022). Some studies on gas generation potential and pore characteristics of Jurassic shales have been performed in China. For example, the Yan'an shale containing type III kerogen in the Ordos Basin has poor to very good hydrocarbon potential, and abundant inorganic pores (Wang et al., 2016). The Badaowan shale containing type III kerogen in the Junggar Basin has fair to good hydrocarbon potential, and abundant intraparticle pores (Gao et al., 2016). The Dameigou shale containing type III kerogen in the Qaidam Basin has good to very good hydrocarbon potential, the pore types were mainly modified mineral pores with isopachous organic matter rims, with pore development affected by TOC and clay mineral content during the early oil and oil window stage (Ko et al., 2016; Liu

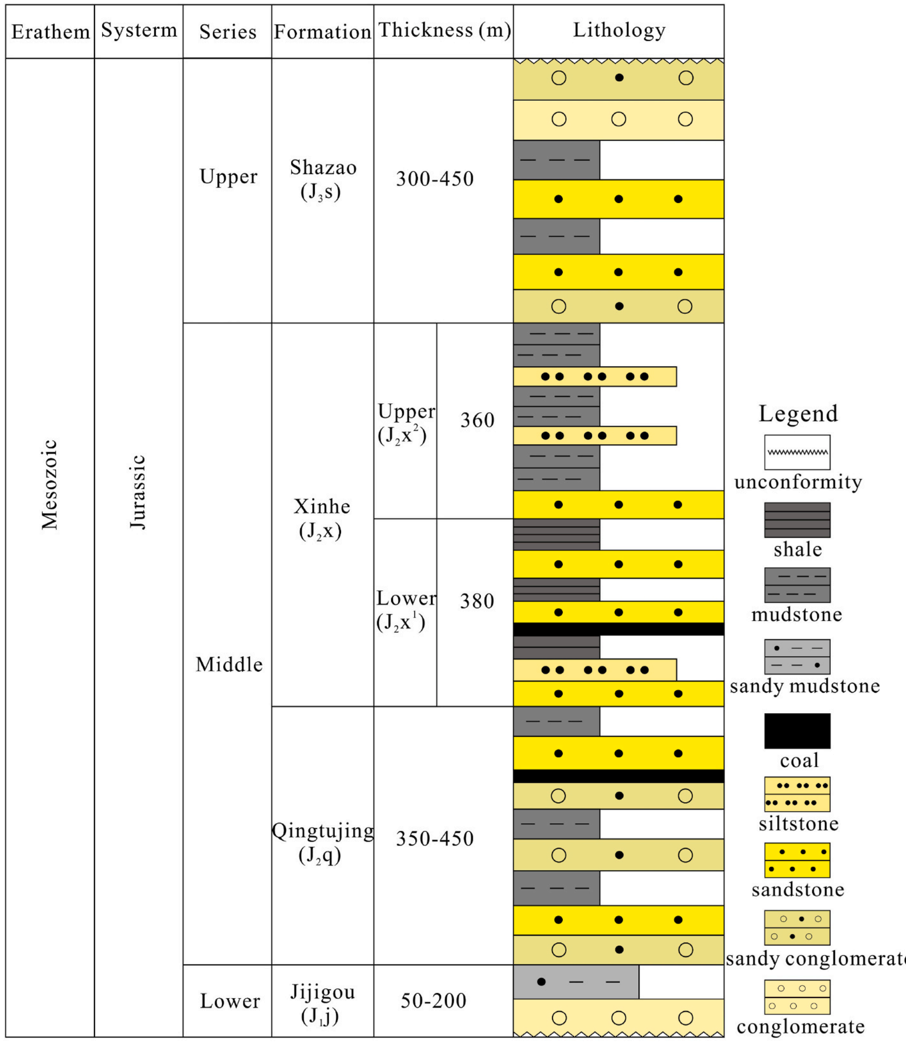

Fig. 2. Generalized stratigraphy and lithology of Jurassic in the Yabulai Basin (modified from Wu et al., 2015).

et al., 2020a). The kerogen of Shimengou shale in the central and northern Qaidam Basin ranges from type I to type III, the pores are characterized as nanopores, micropores and mesopores, with pore development mainly affected by clay minerals (Shao et al., 2014, 2016; Liu et al., 2020b). In the small to moderate basins (such as the Chaoshui and Minhe basins), the pores of continental shale bearing type III kerogen are characterized by interparticle pores between clay platelets and the adsorption capacity of shale is controlled by TOC content (Han et al., 2020).

Gas generation potential is controlled by the abundance of organic matter and adsorption capacity is controlled by surface area (Kim et al., 2017; Han et al., 2020; Li et al., 2023). Analysis of geochemical characteristics of organic matter can provide a framework for shale gas exploration, and analysis of mineral composition and pore structure can provide significant information for hydraulic fracturing (Ye et al., 2022). The organic matter of Jurassic lacustrine source rocks is mainly composed of kerogen types II and III (Burnaz et al., 2022; Li et al., 2023; Wang et al., 2023a, 2023b). However, analysis of pore structures of the Jurassic lacustrine shales mainly focused on type III kerogen (Gao et al., 2016; Han et al., 2020; Liu et al., 2020a, 2020b; Wu et al., 2020), which means that the pore characteristics of Jurassic lacustrine shale containing type II kerogen have not been well documented. As a result, the understanding of gas generation potential and pore characteristics of Jurassic lacustrine source rocks is not comprehensive, which restricts exploration progress.

In this paper, a Jurassic lacustrine shale containing type II kerogen was selected from the Lower Xinhe Formation (J_2x^1) in the Yabulai Basin, northwestern China. Analysis of the geochemical and mineral characteristics are used to evaluate gas generation and fracturing potential of this Jurassic lacustrine shale containing type II kerogen. Analysis of the pore structure and methane adsorption capacity is used to evaluate gas storage capacity of the Jurassic lacustrine shale containing type II kerogen. Based on these experiments, a mathematical model is established to describe the change characteristics of methane adsorption capacity of Jurassic lacustrine shales with depth and TOC content. This research may provide a geochemical reference for the exploration and development of Jurassic lacustrine shale gas and important parameters for the numerical simulation of the shale gas reservoirs in the Yabulai Basin. Moreover, the results of this study also have important reference significance for the relative research of other continental basins with similar geologic conditions, such as other basins belonging to the same basin group as the Yabulai Basin.

2. Geological background and samples

The Yabulai Basin is a Mesozoic-Cenozoic continental rift basin in northwestern China, with an area of 1.5×10^4 km^2 (Zhang et al., 2018). The north of the basin is adjacent to the Ejinaqi Basin, the southwest of the basin is adjacent to the Chaoshui Basin, and the southeast of the basin is adjacent to the Bayanhaote Basin (Fig. 1a). The Yabulai Basin is

Table 1
Geochemical parameters of the Lower Xinhe shale, in the Yabulai Basin.

Sample numbers	Well	Depth(m)	TOC (wt %)	S_1(mg/g)	S_2(mg/g)	T_{max} (°C)	HI (mg/g)	Ro (%)
YBL-1	J1	797.2	2.20	0.14	0.44	434	20	0.65
YBL-2	J1	1060.0	1.62	0.05	1.61	432	99	0.83
YBL-3	YC1	2613.0	1.25	0.39	4.43	442	354	/
YBL-4	YC1	3376.5	1.02	1.37	1.33	432	131	0.75
YBL-5	YC1	3378.0	1.24	0.36	2.52	452	203	/
YBL-6	L1	2268.0	1.06	0.17	1.47	440	139	0.77
YBL-7	L1	2437.0	0.91	0.22	2.63	440	289	0.88
YBL-8	Y1	1349.0	1.10	0.11	2.10	432	191	/
YBL-9	Y1	1582.0	1.17	0.31	3.14	433	268	/
YBL-10	Y1	1786.9	0.59	0.06	0.50	435	85	0.73
YBL-11	HS1	1180.0	2.10	0.12	3.46	436	165	/
YBL-12	HS1	1482.0	1.02	0.06	2.09	438	205	/
YBL-13	YT1	2481.5	1.06	0.38	1.87	440	176	0.86
YBL-14	YT1	2714.8	0.37	0.06	0.56	445	151	0.98
YBL-15	YT2	2090.0	1.88	0.30	5.55	438	395	0.78
YBL-16	YT2	2290.5	1.35	0.13	3.27	440	242	0.83
YBL-17	YT3	816.0	1.96	0.51	11.04	436	563	/
YBL-18	YT3	1325.0	3.26	0.07	2.23	434	68	0.63
YBL-19	YT4	1424.3	9.94	2.78	50.64	437	509	0.78
YBL-20	YT4	1427.3	6.13	2.30	29.67	434	484	0.78
YBL-21	YT4	1429.2	5.12	2.04	22.80	437	445	0.79
YBL-22	YT4	1429.7	9.49	3.61	45.89	434	484	0.79
YBL-23	YT5	2161.0	1.02	0.83	2.86	437	280	/
YBL-24	YT6	2521.6	2.77	0.30	2.37	442	307	0.75
YBL-25	YT6	2952.0	1.67	0.95	2.86	438	171	/
YBL-26	YT6	3560.5	0.19	0.02	0.08	498	42	1.85
YBL-27	YT8	1817.0	31.02	1.13	28.12	439	91	/
YBL-28	YT10	2568.2	5.00	0.52	8.53	435	428	0.77
YBL-29	YT11	2542.7	2.72	0.98	12.42	439	456	0.85
YBL-30	YT11	2569.5	0.35	0.19	0.54	447	154	1.01
YBL-31	YT11	2596.9	0.51	0.23	0.44	454	86	1.12
YBL-32	YT11	2818.3	3.23	1.30	10.57	439	328	0.92
YBL-33	YT11	2824.9	1.59	0.95	3.87	449	243	1.03
YBL-34	YT11	2825.2	2.73	0.34	0.90	451	123	1.01
YBL-35	YT11	2831.7	1.15	8.39	1.35	454	117	0.96
YBL-36	YT11	2851.2	1.34	0.41	1.08	462	81	1.33
YBL-37	YT11	2857.8	0.35	0.41	1.15	459	85	1.15

divided into the Eastern uplift and Western depression. The Western depression is further subdivided into the Hongshanhu sag, Heiciwan low uplift and Saertai sag (Fig. 1b). The samples used in this study were collected from the Saertai sag (Fig. 1b).

Since the Jurassic, the Yabulai Basin has experienced mainly Yanshan and Himalayan movements (Wu et al., 2015). In the Mid-Jurassic, the Saertai sag was the depocenter, forming organic-rich source rocks of the Xinhe and Qingtujing formations. The organic-rich source rocks of the Xinhe Formation were mainly deposited in shallow lacustrine and deep lacustrine settings (Wu et al., 2007, 2015). The Yanshan movements caused the overall uplift of the basin, and exposed Jurassic strata were eroded during the Late Jurassic. After the Late Cretaceous, effected by the Himalayan movements, the southern basin was strongly transformed and the basin area decreased, forming the current tectonic framework.

The stratigraphic section of the Yabulai Basin includes a series of formations ranging in age from Jurassic to Quaternary. The Jurassic strata are composed of Jijigou (J_1j), Qingtujing (J_2q), Xinhe (J_2x) and Shazao (J_3s) formations. The J_2x Formation is further subdivided into Lower Xinhe (J_2x^1) and Upper Xinhe (J_2x^2) members (Fig. 2). Thirty-seven samples were collected from the J_2x^1 member. The J_2x^1 lithology is composed of light-grey sandstone and siltstone, dark-grey shale and coal (Fig. 2).

3. Sample analyses and research methods

3.1. Organic geochemistry

The samples were crushed and sieved to 100 mesh, then 100 mg of powdered sample was treated with 5% HCl at 80 °C to remove carbonates. After the carbonate minerals were fully removed, the residual was washed with distilled water. Treated samples were dried in oven at 80 °C for about 8 h. Iron powder (0.6–1.0 g) and tungsten tin alloy (0.8–1.5 g) were added to each sample as combustion improver, and the TOC contents of samples were measured on the LECO CS230 elemental analyzer with the analytical precision estimated to be 2 ppm.

The S_1 (free hydrocarbon), S_2 (present potential of the source rock) and T_{max} (maximum pyrolysis peak temperature) parameters were measured on a Rock-Eval II instrument. Firstly, a 100 mg powdered sample was heated to 300 °C for 3 min to obtain the S_1, then continue heating to 600 °C at the rate of 25 °C/min to obtain the S_2 and T_{max}. The S_1+S_2 value is used to evaluate the hydrocarbon generation potential. The cross plot of HI (hydrogen index, $HI=S_2 \times 100/TOC$) and T_{max} was used to evaluate the type and maturity of organic matter.

Vitrinite reflectance (R_o) was analyzed using a Lecia DM 4500P multipurpose microscope equipped with 50-X oil immersion objective lens using reflected white light. A reflectance standard (Ro = 0.904%) was used to calibrate the instrument. The Ro value of sample represents the average value of at least 30 points, and the testing standard refers to ASTM D7708-14 (2014) and ISO 7404-5 (2009).

3.2. Reservoir

Mineralogical characteristics of the bulk and clay fraction of the samples were analyzed using X-ray diffraction (XRD). The samples were crushed into fine powder and mounted on X-ray holders. The clay fraction separation was as follows: firstly, about 10 g of extracted sample were transferred to a 100 mL breaker followed by treatment with 0.01 mol/L ethylenediaminetetraacetic acid to remove carbonates and 30% H_2O_2 to remove organic compounds. Then, after the sample was

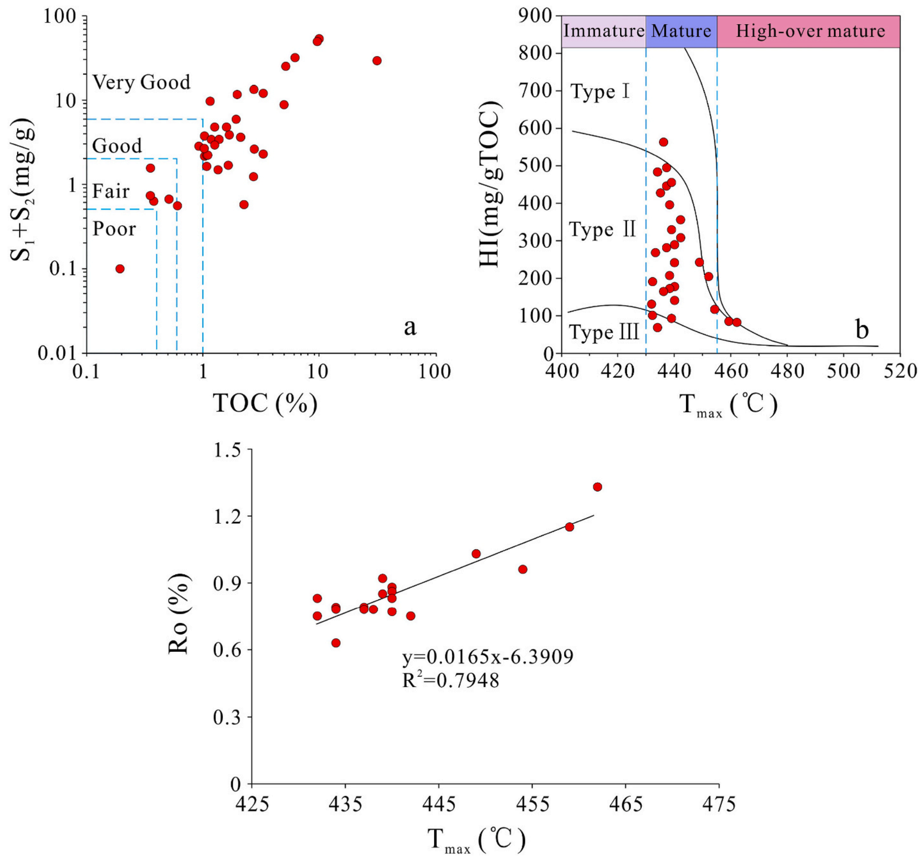

Fig. 3. Geochemical parameters intersection diagram of the Lower Xinhe shales in the Yabulai Basin. (a) S_1+S_2 vs. TOC (after Peters et al., 1986); (b) Ro vs. Tmax; (c) HI vs. Tmax.

completely disaggregated, it was washed with distilled water to confirm complete disaggregation. Finally, the separated clay fraction was placed on a glass slide by pipetting with a dropper and left to dry. The experiment used Cu-Kα radiation generated by 30 Kv and 10 mA. The scans were performed over a 2θ range of 2.5°–80° for the bulk samples and 2.5°–40° for the clay fractions, respectively. More detailed information on the methodology is described in Bhargava et al. (2005).

The porosity and permeability of the samples were analyzed on a PDP 200 instrument. Samples were made into cylinders (diameter: 1.5 cm; length: 2–3 cm). Firstly, the cylinder volume (V_o) is calculated according to the geometric size. Then, the particle volume (V′) was calculated from the experimental results with and without samples. Helium was used as the medium for the experiment. The helium porosity was calculated as follows: $\Phi = (1 - V'/V_o) \times 100\%$. Pulse permeability was calculated using the relationship between the average pressure of upstream and downstream and time. More detailed information on the methodology is described in Han et al. (2020).

The field emission scanning electron microscope (FE-SEM) experiment was completed on the FEI Quanta 200F FE-SEM. Pretreatment before the observation is as follows: (1) the samples were cut into blocks (length: 1 cm; width: 0.5 cm); (2) these cut samples were polished with emery paper; (3) polished samples were argon milled; (4) milled samples were coated with gold.

The low pressure N_2 adsorption experiments were carried out on a Quadrasorb SI surface area instrument. The relative pressure of sample chamber pressure and vapor pressure above the gas (−196.15 °C) increased continuously from 0.05 to 0.99. The Brunauer-Emmett-Teller (BET) method (Brunauer et al., 1938) was used to calculate the specific surface area (SSA) and the Barrett-Joyner-Halenda (BJH) method (Barrett et al., 1951) was used to obtain the pore size distribution of the sample.

The mercury (Hg) intrusion experiment was performed using a PoreMaster 60 GT instrument (U.S). The mercury surface tension, mercury contact angle and sample holder volume are 480 erg/cm^2, 140° and 0.5 mL, respectively. The pressure of mercury continues to increase from 0.14 to 200 MPa. The Washburn equation (Washburn, 1921) was used to calculate the pore diameter of the sample. Testing standard refers to ISO15901-1 (2005). The specific surface area is calculated using the following formula:

$$S = \frac{1}{\gamma/\cos\theta} \int_0^{Vmax} pdV \tag{1}$$

where P is the intrusion pressure, MPa; γ is the surface tension of the intrusion liquid, N/m; θ is the contact angle of the intrusion liquid and the porous medium, degree.

3.3. Methane isothermal adsorption experiment

The FY-KT1000 isothermal adsorption instrument was used to complete the methane isothermal adsorption experiment of the samples. Helium and nitrogen were used to calibrate gas and carrier gas, respectively. Considering the distribution range of the burial depth and corresponding formation temperature in the J_2x^1 shale in the study area, the temperature of each sample was set at 40 °C,50 °C and 60 °C, respectively. The Langmuir volume and pressure of each sample at different temperatures were calculated by the Langmuir equation (Langmuir, 1918).

4. Results and discussion

4.1. Gas generation potential

The basic geochemical parameters of the J_2x^1 shale are shown in Table 1. The TOC and S_1+S_2 values of the J_2x^1 shale range from 0.19% to 31.02% and 0.1 mg/g to 53.42 mg/g (Table 1), with an average of 3.01% and 8.35 mg/g, respectively. The TOC and S_1+S_2 values indicate that most of the J_2x^1 shale can be classified as a very good source rock (Fig. 3a). The Ro value of the J_2x^1 shale sample varies from 0.63% to 1.85%. Ro values indicate that the J_2x^1 shales with low maturity to high-over maturity are distributed across the study area, with most of the J_2x^1 shale in the mature stage. Except for samples with an S_2 value less than 1 mg/g, the HI and T_{max} of range from 68 mg/g to 563 mg/g and 432 °C–462 °C(Table 1) respectively, indicating that the kerogen of these sample is dominated by type II organic matter, with a small amount of typeIand type III kerogen (Fig. 3b). The positive correlation between Ro and T_{max} value indicates that T_{max} value can be used to assess the organic matter maturity of J_2x^1 shale (Fig. 3c). In the cross plot of HI and T_{max}, except for samples YBL-36 and YBL-37 that fall into the high-over mature zone, the J_2x^1 shale samples fall into the mature zone (Fig. 3b), indicating that the thermal evolution of the sample ranges from mature to highly mature, and most of the J_2x^1 shale samples are in the mature stage.

Previous studies have suggested that the enrichment of shale gas is mainly determined by the gas generation potential and storage capacity (Han et al., 2020). The gas generation potential is mainly controlled by organic matter abundance and thermal maturity of source rocks (Jarvie et al., 2007). US exploration practices show that the TOC values of shales that can generate shale gas are generally greater than 2.0% (Jarvie et al., 2007; Ross and Bustin, 2008). The diversity of shale gas genesis indicates that shale gas reservoirs of commercial development scale can be formed at low (Ro $<$ 1.0%) or high maturity (Ro $>$ 2.0%) (Montgomery et al., 2005). Typical low maturity gas reservoirs include Jurassic natural gas in the Turpan-Hami and Santanghu basins of China (Qian et al., 2017). In addition, due to the different activation energy values of different macerals (Sun et al., 1999; Jiang et al., 2005; Xu et al., 2018), different types of organic matter require different maturities when entering the large-scale gas generation stage, and humic kerogen with low activation energy values can provide material foundation for early shale gas generation during the low thermal evolution stage (Galimov, 1988; Zheng et al., 2022). For example, shale gas from the Urengoy gas field is the product of humic organic matter in the Pokur Formation source rocks during low thermal evolution stage (Cramer et al., 1998; Schaefer et al., 1999). The mechanism of early formation of shale gas from humic organic matter is related to the process of condensation of aromatic structures with heteroatomic substitutions (Galimov, 1988; Xu et al., 2009). As the organic matter changes from type I, type II to type III kerogen, the maturity requirement for shale gas generation decreases (Fu, 1990; Zheng et al., 2022). Therefore, considering the shale gas exploration achievements in foreign and the characteristics of continental shale gas reservoirs in China, Luo and Ji (2013) used TOC = 2.0% and Ro = 0.9% as the lower limit to define favorable area for continental shale gas. The thermal simulation experiment results of Jurassic source rocks (type II and III kerogens) in the southern margin of the Junggar Basin also show that the source rocks enter the stage of rapid gas generation and expulsion when the Ro $>$ 0.9% (Ma et al., 2020). The abundance and thermal maturity of organic matter in most of the J_2x^1 shale have reached the lower limit of shale gas favorable area evaluation.

Affected by the tectonic evolution, the depocenter of the basin migrated eastward during the sedimentary period of the J_2x^1, resulting in a decrease in shale thickness in the Saertai sag from east to west. The cumulative thickness of the J_2x^1 shale ranges from 396 m to 1174 m, the maximum thickness of shale single layer exceeding 50 m (Wang, 2014), which is greater than the lower limit (30 m) of continuous thickness of

Table 2
Mineralogical composition of the Lower Xinhe shale, in the Yabulai Basin.

Sample numbers	Well	Depth (m)	Mineral composition (%)									Clay composition (%)				Brittleness index
			Quartz	Feldspar	Calcite	Ankerite	Analcime	Augite	Pyrite	Siderite	Clays	I/S	Illite	Kaolinite	Chlorite	
YBL-4	YC1	3376.5	16.1	10.8	6.3	10.9	/	/	/	/	55.9	58	31	0	11	0.44
YBL-10	Y1	1786.9	22.8	31	/	/	/	/	/	/	46.2	23	44	6	27	0.54
YBL-19	YT4	1424.3	29.4	11.2	/	/	/	/	/	/	59.4	78	15	4	3	0.41
YBL-20	YT4	1427.3	19.0	10.3	11.9				8.4	4.4	45.9	68	21	7	4	0.50
YBL-21	YT4	1429.2	18.1	8	12.4	15.2	/	/	/	10.2	36.1	63	24	8	5	0.64
YBL-22	YT4	1429.7	20.7	11.2	18.1	/	/	/	/	/	50	/	/	/	/	0.50
YBL-24	YT6	2521.6	22.5	7.3	8.9	/	/	/	/	/	61.3	84	0	4	12	0.39
YBL-28	YT10	2568.2	13.4	4.4	6.3	/	3.7	/	/	33.4	38.8	88	0	5	7	0.60
YBL-29	YT11	2542.7	\	38.2	7.6	29.5	/	/	/	/	24.7	24	43	19	13	0.75
YBL-30	YT11	2569.5	9.1	16.5	6.8	15.4	6.0	/	/	/	46.1	1	81	2	16	0.51
YBL-31	YT11	2596.9	7.4	17.7	5.5	/	5.3	/	/	17.9	64.1	10	62	8	20	0.43
YBL-32	YT11	2818.3	14.4	3.9	4.9	16.6	/	14.4	1.3	/	44.5	0	93	4	3	0.47
YBL-33	YT11	2824.9	19.0	15.6	12.3	4.5	/	/	/	/	48.5	56	40	0	4	0.51
YBL-34	YT11	2825.2	16.1	13.5	22.6	/	/	/	/	/	47.8	72	20	2	6	0.52
YBL-35	YT11	2831.7	20.7	7.7	14	/	/	/	/	5.5	52.1	65	23	4	8	0.48
YBL-36	YT11	2851.2	20.3	8.1	3.1	/	/	/	/	3.2	65.3	71	11	10	8	0.35
YBL-37	YT11	2857.8	20.8	4.7	2.8	/	/	/	/	/	71.7	52	45	1	2	0.28

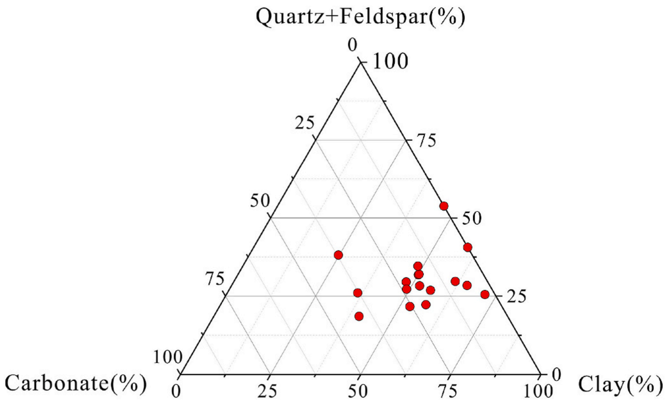

Fig. 4. Ternary diagram of the mineralogical compositions of the Lower Xinhe shale in Yabulai basin.

shale in the evaluation criteria of continental shale gas favorable area (Zou et al., 2010; Luo and Ji, 2013). In addition, previous studies show that the thermal evolution of most of the J_2x^1 source rocks in the Yabulai Basin have reached the peak stage of hydrocarbon generation, with a total hydrocarbon generation of about 42.5×10^9 t (Wang, 2014; Dong, 2014). Affected by the low thermal maturity of the source rocks in this member, the gas generation of most J_2x^1 shale cannot meet the basic adsorption requirements of reservoirs pores (Dong, 2014; Tian, 2015), so most of the shale gas are distributed in the pores of shale and adjacent sandstone. The results of canister desorption indicate that the gas contents of the J_2x^1 shale is 0.67 m^3/t (Han et al., 2014), which is close to the Lewis Shale (0.42–1.27 m^3/t) (Curtis, 2002). Therefore, the J_2x^1 shale has good gas exploration potential in the study area.

4.2. Mineral composition

The mineral components of the J_2x^1 shale in the Yabulai Basin are shown in Table 2 and Fig. 4. The mineralogical compositions of these samples are mainly clays (24.7–71.7%, average value = 50.5%) and quartz (0–29.4%, average value = 17.1%), followed by feldspar (3.9–38.2%, average value = 12.9%), calcite (0–22.6%, average value = 8.4%), ankerite (0–29.5%, average value = 5.8%) and siderite (0–33.4%, average value = 4.4%). The contents of analcime, augite and pyrite are relatively low. The brittleness index ((quartz + feldspar + carbonate)/(quartz + feldspar + carbonate + clay) (Zou et al., 2010) of the samples varies from 0.28 to 0.64 (Table 2), with an average of 0.49. A value of 0.4 is generally considered to be the threshold of brittle mineral content for effective hydraulic fracturing (Jarvie et al., 2007), therefore, the J_2x^1 shale in the Yabulai Basin has good hydraulic fracturing potential.

4.3. Pore structure and control factors

Helium porosity and pulse permeability of the J_2x^1 shale samples are shown in Table 3. The porosity and permeability of these samples ranged from 3.00% to 3.54% and from 0.00020 mD to 0.00052 mD (Table 3), respectively. Compared other porosity and permeability characteristics of shale gas reservoirs, the J_2x^1 shale has relatively high porosity and permeability. For example, the J_2x^1 shale has higher porosity than the Chang 7 shale (0.15–3.42%) and the Yan'an shale (2.01–2.92%) in the Ordos Basin, and higher permeability than the Barnett Shale (0.00010–0.00025 mD) in the Fort Worth Basin and the Woodford Shale (0.0001–0.0002 mD) in the Arkoma Basin (Curtis, 2002; Wang et al., 2016; Han et al., 2020) (Table 3). The relatively high permeability of the J_2x^1 shale indicates that the connection between pores is good, which is conducive to the migration and accumulation of oil and gas. The relatively high porosity provides sufficient accommodation space for oil and gas. Moreover, hydraulic fracturing can also further improve the permeability and enhance the connectivity of the J_2x^1 shale. Therefore, the porosity and permeability characteristics of the J_2x^1 shale have the conditions to form large shale gas reservoirs.

The pores of shale are generally divided into interparticle, intraparticle and organic pores (Loucks et al., 2012). Based on formation mechanism of mineral pores, the interparticle pores and intraparticle pores of shale can be further divided into residual interparticle pores, interparticle dissolution pores, residual intraparticle pores and intraparticle dissolution pores (He et al., 2017). Different from the pore characteristics of Jurassic shale containing type III kerogen in the Junggar and Qaidam basins (Gao et al., 2016; Han et al., 2020; Liu et al., 2020a, 2020b; Wu et al., 2020), a large number of interparticle dissolution pores and organic pores were observed in the J_2x^1 shale in the Yabulai Basin, in addition to the residual interparticle pores between clay platelets (Fig. 5a).

The interparticle dissolution pores are distributed in clay (Fig. 5b–d) or along the edge of organic matter (Fig. 5e). The dimensions of the interparticle dissolution pores ranges from 3.8 nm to 14 μm. The size of the organic pores varies from 27 nm to 501 nm (Fig. 5f–h). Moreover, microfractures were also observed in the J_2x^1 shale, the lengths of the microfractures are greater than 4 μm and widths are greater than 250 nm (Fig. 5h). The development of microfractures distributed along organic matter in the J_2x^1 shale can significantly improve the fracturing effect (Chen et al., 2021b). On the whole, the pores of the J_2x^1 shale containing type II kerogen in the Yabulai Basin are mainly composed of residual interparticle pores, interparticle dissolution pores and organic pores. The majority of pores in the Jurassic continental shale are inorganic pores with a small percentage of organic pores in the Yuka depression of the Qaidam and Chaoshui basins (Liu et al., 2020a; Han et al., 2020). Different from the Jurassic continental shale in the Yuka depression of the Qaidam and Chaoshui basins, the pore composition of the J_2x^1 shale containing type II kerogen in the Yabulai Basin contains a

Table 3
Helium porosity and plus permeability of shale samples in the Yabulai Basin and other basins.

Basin	shale	Sample	Well	Depth (m)	Ro (%)	Porosity (%)	Permeability (mD)
Yabulai	Xinhe member	YBL-4	YC1	3376.5	0.75	3.35	0.00015
		YBL-19	YT4	1424.3	0.78	3.54	0.00020
		YBL-21	YT4	1429.2	0.79	3.41	0.00043
		YBL-24	YT6	2521.6	0.75	3.20	0.00032
		YBL-28	YT10	2568.2	0.77	3.52	0.00039
		YBL-32	YT11	2818.3	0.92	3.29	0.00051
		YBL-34	YT11	2825.2	1.01	3.31	0.00026
		YBL-35	YT11	2831.7	0.96	3.15	0.00052
		YBL-36	YT11	2851.2	1.33	3.25	0.00034
		YBL-37	YT11	2857.8	1.15	3.00	0.00045
Ordos	Yan'an	/	/	/	0.4–0.7	2.01–2.92	0.041–0.067
	Chang 7	/	/	/	0.52–1.25	0.15–3.42	/
Fort Worth	Barnett	/	/	/	1.0–1.3	4.00–5.00	0.00010–0.00025
Arkoma	Woodford	/	/	/		/	0.0001–0.0002

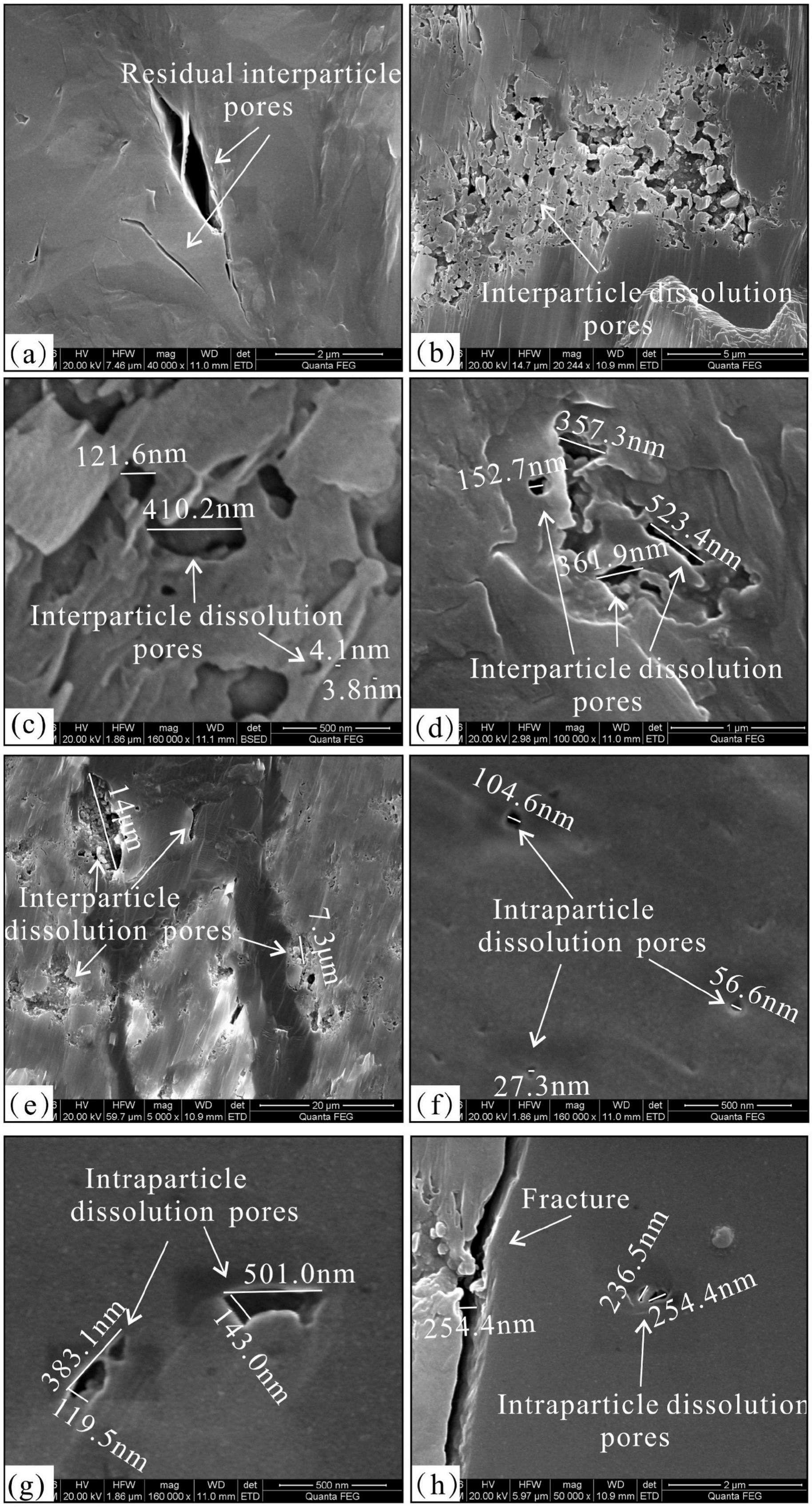

Fig. 5. The SEM images of the Lower Xinhe shale in the Yabulai ((a) YBL-19; (b) YBL-27; (C) YBL-22; (d) YBL-19; (e) YBL-27; (f): YBL-18; (g) YBL-19; (h): YBL- 19).

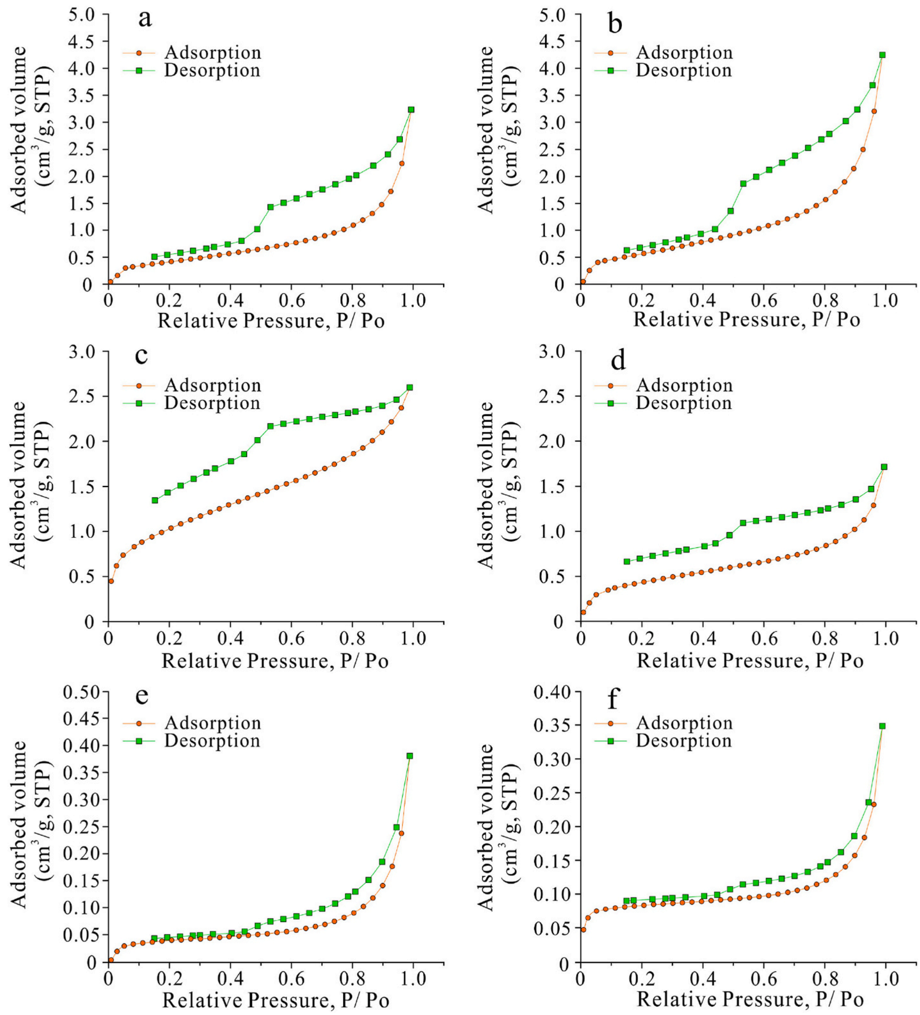

Fig. 6. The adsorption/desorption isothermal curves of the Lower Xinhe shale in the Yabulai Basin (a. YBL-18; b. YBL-19; c. YBL-22; d. YBL-26; e. YBL-27; f. YBL-29).

large number of organic matter pores (Fig. 5). Moreover, the size of interparticle dissolution pores in the J_2x^1 shale containing type II kerogen in the Yabulai Basin is similar to that of the Jurassic continental shale in Chaoshui Basin (Han et al., 2020), but larger than that of the Jurassic continental low-maturing shale in the northern margin of the Qaidam Basin (Zhang et al., 2021).

The experimental results of low-pressure N_2 adsorption and desorption isotherms of the J_2x^1 shale are shown in Fig. 6. The adsorption curves of the J_2x^1 shales are characterized by a reversed S shape, and belong to the type II isotherms (Brunauer, et al., 1940; Sing, 1982), indicating that there is multilayer adsorption in these samples and that the surface area can be calculated using the BET theory (Gregg and Sing, 1982). Moreover, the adsorption curves increased rapidly when the relative pressure (P/Po) was greater than 0.9, indicating that there is a small amount of macropores in the J_2x^1 shale and a large amount of micropores and mesopores (Gregg and Sing, 1982). When $P/Po > 0.45$, the desorption curves are above the adsorption curves in the J_2x^1 shale (Fig. 6). When $P/Po < 0.45$, the desorption curves basically overlap with the adsorption curves in the J_2x^1 shale (Fig. 6a, b, e, f). The hysteresis phenomenon of the desorption curve when P/Po is greater than 0.45 is related to the capillary condensation in the desorption process (Barsotti et al., 2016). The hysteresis loops of the J_2x^1 shale are characterized by type H4 hysteresis (Fig. 6a, b, e, f) (Sing, 1982), suggesting that pores may be characterized as slit-typed pores. In addition, these adsorption curves have forced closure phenomenon when the relative pressure is about 0.45, indicating that the shale also contains flask shaped ink bottle pores (Li et al., 2019). The hysteresis curves of YBL-22 and YBL-26 are not closed when $P/Po < 0.45$ (Fig. 6c and d), which is related to swelling or nitrogen molecule adsorption in micropores (Gregg and Sing, 1982).

Table 4
Total pore volume and specific surface area of the Lower Xinhe shale in the Yabulai Basin.

Sample	Total pore volume (cm^3/g)		Specific surface area (m^2/g)	
	N_2 adsorption	Mercury intrusion	N_2 adsorption	Mercury intrusion
YBL-19	0.01090	nd	6.521	nd
YBL-21	0.00657	0.00440	2.077	1.29
YBL-24	0.00402	0.00220	3.739	0.78
YBL-28	0.00265	0.00300	1.594	0.90
YBL-32	0.00159	0.00095	1.139	0.60
YBL-35	0.00053	0.00090	0.152	0.09

The volume and surface area data of the J_2x^1 shale in the Yabulai Basin are shown in Table 4. The total pore volume of the J_2x^1 shale obtained by the N_2 adsorption experiment and mercury intrusion experiment varies from 0.00053 cm^3/g to 0.01090 cm^3/g and from 0.00090 cm^3/g to 0.00440 cm^3/g, respectively. The BET surface area obtained by the N_2 adsorption experiment ranges from 0.152 cm^3/g to 6.521 m^2/g, with the specific surface area obtained by mercury intrusion experiments ranging from 0.09 cm^3/g to 1.29 m^2/g. The dv/dD diagram shows that the pore size of the J_2x^1 shale is characterized by near 4 nm

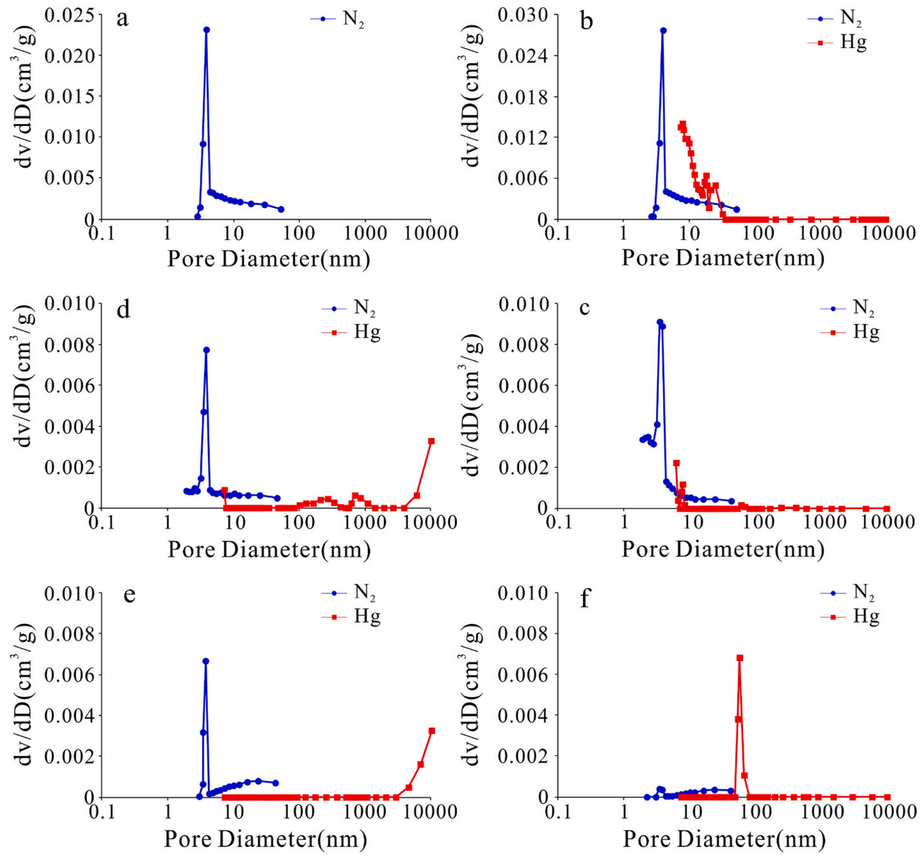

Fig. 7. Pore size distributions of the Lower Xinhe shale from N_2 adsorption and mercury intrusion experiments (a. YBL-18; b. YBL-19; c. YBL-22; d. YBL-26; e. YBL-27; f. YBL-29).

(Fig. 7), 58 nm (Fig. 7f), and >10 μm (Fig. 7d,e). According to the dimension of the pores, the pores can be divided into micropores (<2 nm), mesopores (2–50 nm) and macropores (>50 nm) following Rouquerol et al. (1994). Thus, pores of the J_2x^1 shale are dominated by mesopores and macropores.

There is a positive correlation between porosity and TOC content in the J_2x^1 shale (Fig. 8a), which has also been observed in the Marcellus Formation of Pennsylvania (Milliken et al., 2013). The porosity of the J_2x^1 shale increases rapidly when TOC<2.0%, and slowly when TOC>2.0% (Fig. 8a). This is because the higher the TOC content, the greater the number of organic pores and the greater the porosity. However, when the TOC content is too high, mechanical compaction results in organic matter compression and deformation, resulting in the closure or reduction of organic pores (Curtis et al., 2012; Wang et al., 2023a). The positive correlation indicates that there are a large number of pores associated with the organic matter, which is consistent with the results observed using FE-SEM (Fig. 5f–h). The porosity of the J_2x^1 shale decreases with an increase of T_{max} (Fig. 8b), which is related to the destruction of pores during compaction (Dang et al., 2018). Moreover, negative correlations can be seen between porosity and quartz and clay contents (Fig. 8c, d), while a positive correlation can be seen between porosity and carbonate content (Fig. 8e). The relatively high content of brittle minerals and low content of clay minerals improves the anti-compression strength of shale, which is conducive to the formation of inorganic pores such as interparticle and intraparticle pores. The correlation between porosity and quartz, clay and carbonate content of the J_2x^1 shale indicates that the inorganic pores in clay and carbonate minerals provide the main pore space. Sample YBL-18 deviated from the trend in Fig. 8c–e, which is mainly related to low carbonate content. Therefore, the organic matter abundance and thermal maturity, as well as mineral composition have significant influence on the porosity of the J_2x^1 shale, and the contribution of pores mainly comes from organic pores related to organic matter and inorganic pores related to clay and carbonate minerals.

The pore volume and specific surface area of the J_2x^1 shale are positively correlated with TOC content (Fig. 9a–d), indicating that organic pores account for a large proportion of the pores in the J_2x^1 shale. For example, the mineral compositions of the YBL-19 and YBL-29 are basically the same, but the TOC content of YBL-19 is higher than YBl-29, and the pore volume and specific surface area of the YBL-19 are higher than that of YBL-29. The BET surface area and pore volume of low-pressure N_2 adsorption show a trend of first increasing and then decreasing with T_{max} values (Fig. 9e and f), which may be related to the formation of organic pores at low maturity stage (Wang et al., 2022) and the collapse and filling of organic pores at high maturity stage (Zhao et al., 2016; Zhang et al., 2017). The BET surface area and pore volume of low-pressure N_2 adsorption are weakly negatively correlated with carbonate content (Fig. 9g and h) and weakly positively correlated with clay content (Fig. 9i and j), indicating that inorganic pores account for a small proportion in the pores of the J_2x^1 shale. These characteristics indicate that the TOC content has a significant impact on the pore structure of the J_2x^1 shale.

4.4. Adsorption capacity and control factors

The characteristics of the methane isothermal adsorption curves of the J_2x^1 shale are similar and belong to type I variety (Fig. 10). The methane adsorption capacity of the J_2x^1 shale gradually increases with the increase of pressure at the same temperature, while the methane adsorption capacity of the J_2x^1 shale decreases with the increase of temperature at the same pressure (Fig. 10 and Table 5). The results show that the methane adsorption capacity of the J_2x^1 shale is affected by

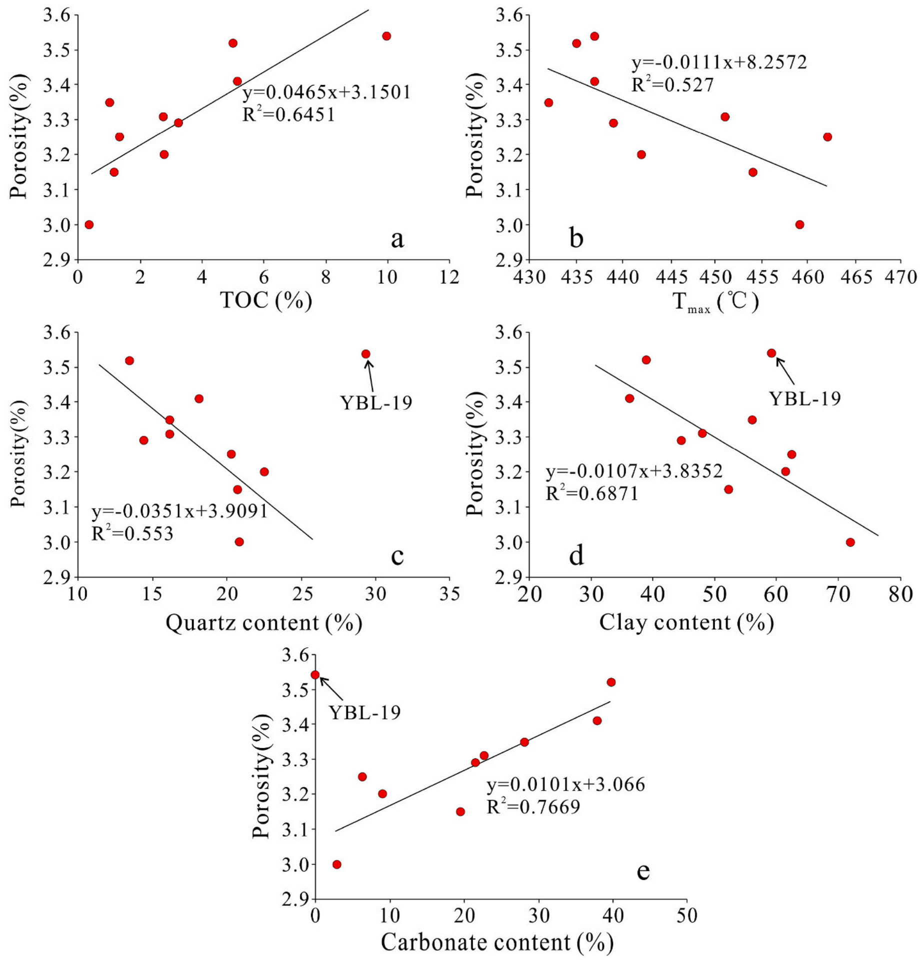

Fig. 8. Porosity vs. TOC (a), Tamx (°C) (b), quartz content (c), clay content (d) and carbonate content (e) of the Lower Xinhe shale in the Yabulai Basin.

pressure and temperature. The volume and pressure of the sample calculated according to the Langmuir equation (Langmuir, 1918) are shown in Table 5. The Langmuir volumes of the J_2x^1 shale display a range of 2.10–2.99 m^3/t and average 2.53 m^3/t, which is higher than the Lower Cretaceous shales in Canada (Chalmers and Bustin, 2007) and Qiongzusi shales in Sichuan Basin (Wang et al., 2013). This indicates that the J_2x^1 shale has a relatively good gas storage capacity.

The residual interparticle, interparticle dissolution and organic pores in the J_2x^1 shale provide a large number of sites for gas adsorption. Moreover, the microfractures distributed along organic matter can also be used to adsorb the gas in the J_2x^1 shale, Yabulai Basin. The methane adsorption capacity of the J_2x^1 shale (type II kerogen) is directly proportional to TOC content, with an R^2 value of 0.7437 (Fig. 11a), which has been observed in the Eocene Green River Shale (typeIkerogen), Devonian–Mississippian Woodford Shale (type II keorgen), the Chang 7 Member (the seventh member of Yanchang Formation) shale (type II kerogen) in the Ordos Basin and the Jurassic J_2x^1 shale (type III kerogen) in the Yabulai Basin (Zhang et al., 2012; Xing et al., 2018; Han et al., 2020). The methane adsorption capacity of the J_2x^1 shale is inversely proportional to clay content, with an R^2 value of 0.7622 (Fig. 11b). The clay composition of the J_2x^1 shale is composed of illite-smectite and illite (Table 2), the surface area of smectite (800 m^2/g) is much higher than that of illite (30 m^2/g), and the pore volume is generally directly proportional to surface area (Ross and Bustin, 2009; Passey et al., 2010). Moreover, the enrichment of organic matter also reduces the specific surface area of clay minerals, resulting in the reduction of gas adsorption sites (Ji et al., 2015; Gao et al., 2017). Therefore, the negative correlation between the methane adsorption capacity and clay content in the J_2x^1 shale may be related to the high content of illite-smectite and illite in clay minerals and the strong effect of TOC. In summary, the methane adsorption capacity of the J_2x^1 shale in the Yabulai Basin is strongly controlled by the TOC and clay mineral contents. Moreover, the methane adsorption capacity of the J_2x^1 shale is inversely proportional to the temperature and pressure, with an R^2 values of 0.889–0.997 and 0.8169–0.9683 (Fig. 11c and d), respectively, indicating that the methane adsorption capacity of the J_2x^1 shale in the Yabulai Basin decreases with increasing temperature (maturity) and pressure.

4.5. Prediction of adsorption capacity

The prerequisites for comprehensive analysis of shale gas exploration potential are favorable geochemical conditions and rocks with sufficient gas adsorption capacity and potential for fracturing. Most of the J_2x^1 shale in the Yabulai Basin can be classified as a very good source rock, and the kerogen type is dominated by type II (Fig. 3). The J_2x^1 shale has a moderate maturity, corresponding to the main hydrocarbon generation window. The source rocks dominated by type II/III kerogen can generate gas at a relatively low thermal evolution stage (Galimov, 1988; Wang et al., 2010). Therefore, there are abundant shale gas resources in J_2x^1 shale reservoir in the Yabulai Basin, which has been suggested by the desorption results of fresh shale samples (Han et al., 2014). For a given sedimentary basin, the hydrocarbon generation conditions of shale gas, such as organic matter abundance, kerogen type and maturity of source rocks, have been determined, so the scale of the shale gas reserves mainly depend on methane adsorption capacity.

As mentioned above, the adsorption capacity of the J_2x^1 shale (type

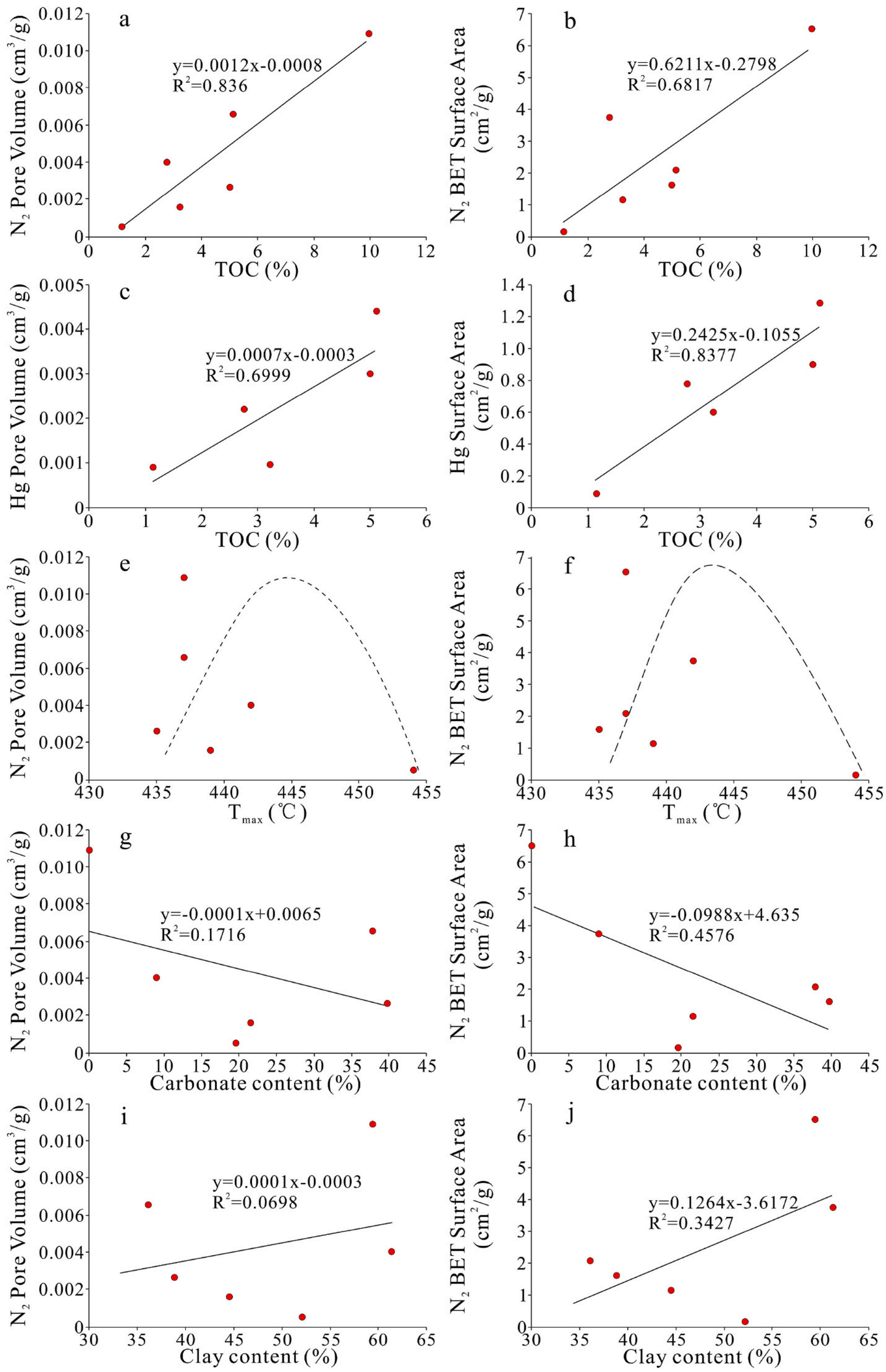

Fig. 9. Pore volume and surface area vs. TOC, carbonate and clay contents of the Lower Xinhe shale in the Yabulai Basin.

II) is controlled by TOC content, clay mineral content, temperature and pressure. Therefore, based on these experimental data of the J_2x^1 shale in this study and previous studies (Han et al., 2020), the relationship between the Langmuir volume, TOC content, clay mineral content and temperature of the J_2x^1 shale containing type II kerogen in the Yabulai Basin was established using correlation and regression analysis. The expression is as follows:

$$V_L = 0.866 \times TOC + 0.053 \times CM - 0.05 \times T - 0.651 \quad R^2 = 0.8494 \tag{2}$$

V_L: Langmuir volume, m^3/t; TOC: total organic carbon content, %; CM: the content of clay minerals, %; T: temperature, °C. The calculated Langmuir volume of the J_2x^1 shale was directly proportional to its measured Langmuir volume, with an R^2 value of 0.8476 (Fig. 12a), which shows that calculation model is reliable.

The clay mineral content of the J_2x^1 shale containing type II kerogen in the Yabulai Basin was inversely proportional to TOC content, with an R^2 value of 0.9167 (Fig. 12b). Thus, the relationship between the clay mineral and TOC contents of the J_2x^1 shale containing type II kerogen was established using correlation and regression analysis. The expression is as follows:

$$CM = -8.9116 \times TOC + 80.852 \quad R^2 = 0.9167 \tag{3}$$

CM: the content of clay minerals, %; TOC: total organic carbon content, %.

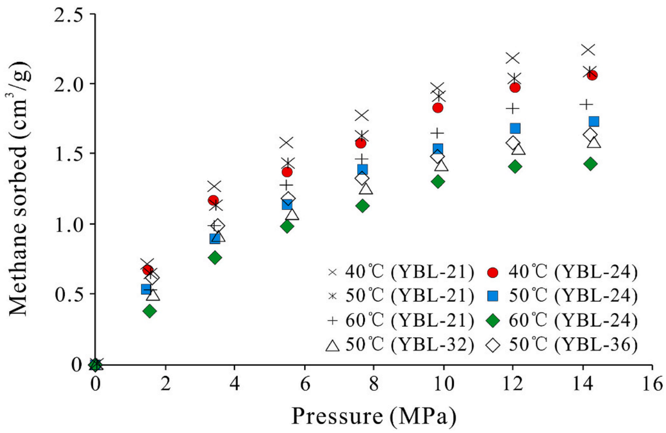

Fig. 10. Methane isothermal adsorption for the Lower Xinhe shale in Yabulai Basin.

Table 5
Langmuir parameters for the Lower Xinhe shale in the Yabulai Basin.

Sample	Temperature (°C)	Langmuir volume (m^3/t)	Langmuir pressure (MPa)
YBL-21	40	2.99	4.85
	50	2.93	5.58
	60	2.68	6.09
YBL-24	40	2.73	4.90
	50	2.42	5.63
	60	2.16	6.78
YBL-32	50	2.19	5.45
YBL-36	50	2.10	4.07

In addition, the natural logarithm of the Langmuir pressure is directly proportional to temperature, with an R^2 value of 0.8108 (Fig. 12c). Therefore, the relationship between the Langmuir pressure and temperature of the J_2x^1 shale was established using correlation and regression analysis. The expression is as follows:

$$\ln (P_L) = 0.032 \times T + 0.0361 \quad R^2 = 0.8108 \tag{4}$$

P_L: Langmuir pressure, MPa; T: temperature, °C.

Bringing Eq. (2), Eq. (3) and Eq. (4) into the Langmuir equation, a mathematical model is established to describe the influence of TOC content, clay mineral content, temperature and pressure on the gas adsorption capacity of the J_2x^1 shale in the Yabulai Basin. The expression is as follows:

$$V = \frac{(0.394 \times TOC - 0.05 \times T + 3.634) \times P}{P + e^{(0.032 \times T + 0.0361)}} \tag{5}$$

V: methane adsorption amount, m^3/t; T: temperature, °C; P: pressure under geological condition, MPa. The model of methane adsorption capacity not only predicts the methane adsorption capacity of the J_2x^1 shale in the Yabulai Basin under current geological conditions, but also reconstructs the dynamic evolution process of methane adsorption capacity of the shale reservoir in geological history.

Assuming that the J_2x^1 shale gas is composed of methane, Eq. (5) can be used to calculate adsorption amount of the J_2x^1 shale under given geological conditions. The surface temperature and geothermal gradient are 10 °C and 2.7 °C/100m (Tian et al., 2015), respectively. The hydrostatic pressure gradient is 10.5 MPa/km (Ma et al., 2016). The variation in adsorption capacity of the J_2x^1 shale with depth and TOC content are shown in Fig. 13. The methane adsorption capacity of the J_2x^1 shale first increases and then decreases with increasing depth, and the depth corresponding to the maximum methane adsorption increases with increasing TOC content. The maximum adsorption amount of the J_2x^1 shale appears at 400–800 m when the TOC contents vary from 1% to 10%. Above the maximum value, the positive impact of formation pressure is greater than the negative effect of formation temperature on methane adsorption capacity, resulting in the increase of methane adsorption capacity with increasing depth. Below the maximum value the condition is reversed (Ji et al., 2014; Xing et al., 2018). In addition, when the TOC contents vary from 1% to 10%, the minimum adsorption amount of the J_2x^1 shale appears below 2600 m, and the depth corresponding to the minimum methane adsorption amount increases with increasing TOC content. The adsorption amount of the J_2x^1 shale tends to disappear at a depth range of 2600–5100m, which is mainly related to high formation temperature and pressure. When the burial depth is greater than the depth corresponding to the minimum adsorption amount, due to the high formation temperature and pressure, the shale

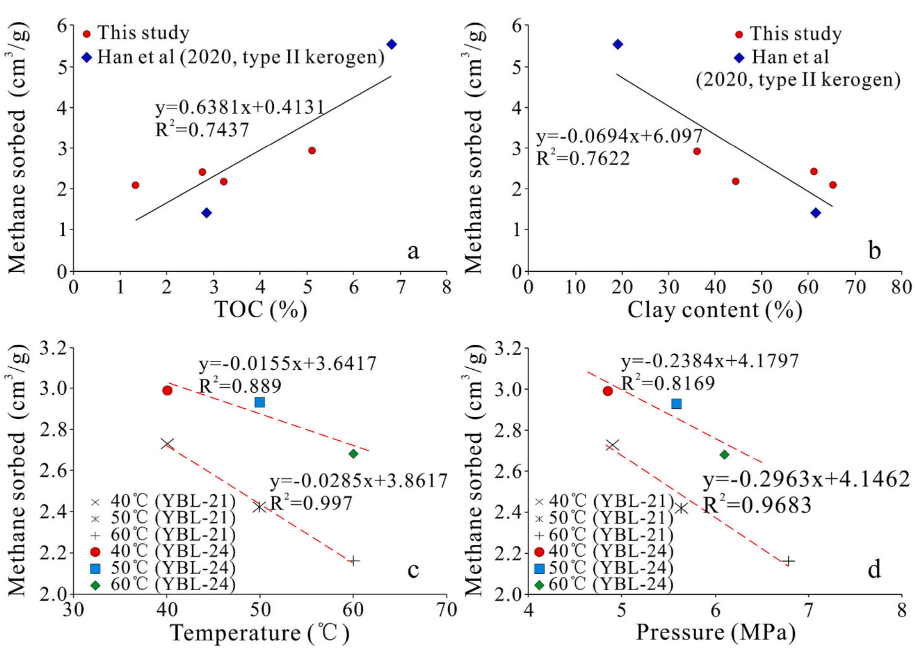

Fig. 11. Methane isothermal adsorption capacity vs. TOC and clay content (a, b), and methane isothermal adsorption capacity vs. temperature and pressure of the Lower Xinhe shale in the Yabulai Basin.

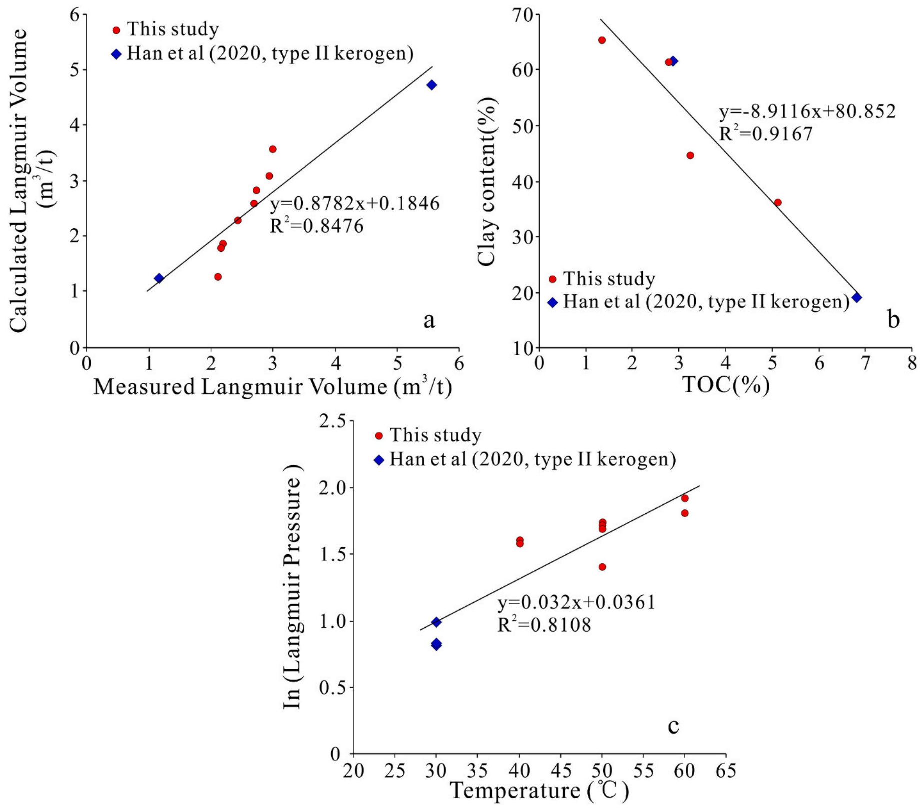

Fig. 12. The Calculated adsorption volume vs. measured adsorption volume (a), clay content vs. TOC content (b), and Ln (Langmuir Pressure) vs. Temperature (c) of the Lower Xinhe shale in Yabulai Basin.

adsorption capacity begins to decrease significantly, the free gas content beings to exceed the adsorption gas content, and the shale gas is dominated by free gas. For example, the shale gas is dominated by adsorbed gas shallower than 2600m when the TOC content of the J_2x^1 shale is 1%, and the shale gas is dominated by free gas deeper than 2600m, and the favorable shale gas exploration depth of the J_2x^1 shale in the study area is deeper than 2600m (Fig. 13). The shale gas is dominated by adsorbed gas shallower than 5100m when the TOC content of the J_2x^1 shale is 10%, and the shale gas is dominated by free gas deeper than 5100m, and the favorable shale gas exploration depth of the J_2x^1 shale in the study area is deeper than 5100m. In summary, the depth corresponding to the minimum adsorption amount increases with increasing TOC content, resulting in the favorable shale gas exploration depth of the J_2x^1 shale in the study area increasing with increasing TOC content.

As mentioned above, the TOC values of the J_2x^1 shale range from 0.19% to 31.02% (Table 1 and Fig. 3a), with an average value of 3.01%. When the TOC content is 3.01%, according to the predictive model for methane adsorption amount of the J_2x^1 shale (Eq. (5)), the methane adsorption capacity of the shale first increases and then decreases with increasing depth, reaching its maximum value at 500m (Fig. 13). The total shale gas is dominated by adsorbed gas shallower than 3200m, and the shale gas is dominated by free gas deeper than 3200m. The favorable shale gas exploration depth of the J_2x^1 shale in the study area is deeper than 3200m. In addition, for other continental basins with similar geological conditions, such as Chaoshui and Bayanhaote basins in northwestern China (Li et al., 2016), a predictive model for shale methane adsorption capacity can be established using this approach, reflecting the dynamic evolution of shale methane adsorption capacity with depth and TOC content.

5. Conclusion

The J_2x^1 shale is mainly classified as a very good source rock. Kerogen is dominated by type II organic matter with thermal evolution ranging from mature to highly over-mature. The content of brittle minerals is high and has good hydraulic fracturing potential. The methane adsorption capacity is in the range of 2.10–2.99 m^3/t, which is higher than other gas shales. The geochemical parameters and methane adsorption capacity suggest that the J_2x^1 shale has good shale exploration and development potential.

Compared with the Jurassic shale containing type III kerogen, there are not only residual interparticle pores between clay platelets, but also a large number of interparticle dissolution pores in clay minerals and organic pores in the J_2x^1 shale. In addition, there are microfractures along the edge of organic matter in the J_2x^1 shale. Pores and microfractures provide sufficient sites for shale gas adsorption in the J_2x^1 shale. The pores of the J_2x^1 shale are dominated by mesopores and macropores, and the TOC content has a significant impact on the porosity and pore structure of the J_2x^1 shale.

The methane adsorption capacity of the J_2x^1 shale is mainly affected by TOC content, clay mineral content, temperature and pressure. A mathematical model for the variation of methane adsorption capacity with depth and TOC content in the J_2x^1 shale is established. The methane adsorption capacity of the J_2x^1 shale first increases and then decreases with the increase of depth, and the depth corresponding to the maximum methane adsorption increases with increasing TOC content. When TOC contents vary from 1% to 10%, the maximum value of adsorbed amount of the J_2x^1 shale appears at 400–800 m, and the adsorption amount of the shale tends to disappear at a depth range of 2600–5100 m. The favorable shale gas exploration depth of the J_2x^1 shale in the study area increases with increasing TOC content.

The research results provide geochemical references for the J_2x^1 shale gas exploration in the Yabulai Basin, and are of significance for

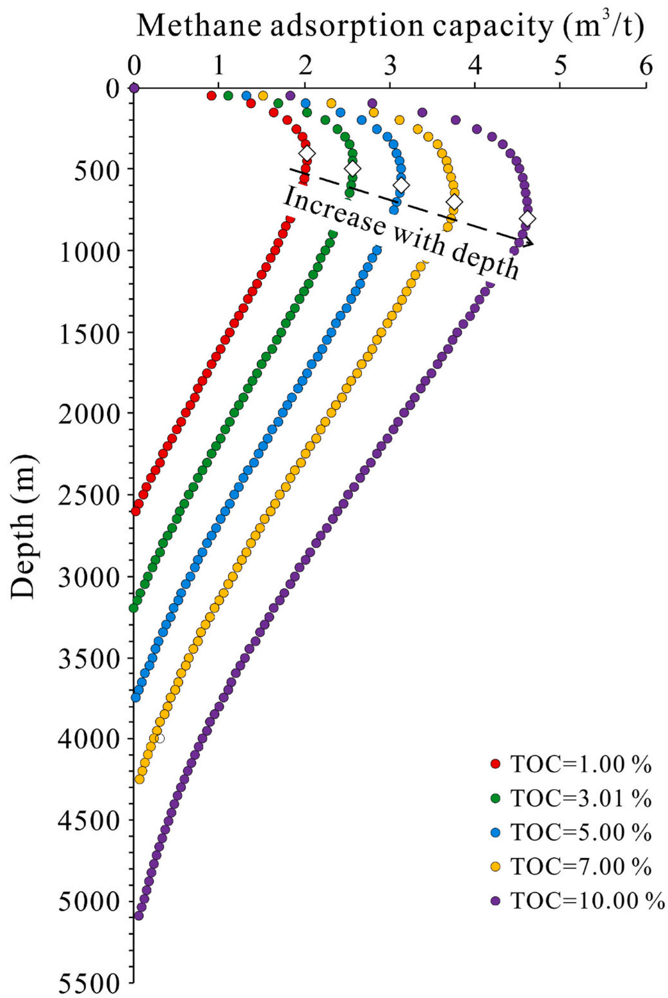

Fig. 13. Variation of methane adsorption capacity of the Lower Xinhe shale with depth and TOC content calculated by Eq. (5) in Yabulai Basin.

Jurassic shale gas exploration in other continental basins with similar geologic conditions such as the Chaoshui and Bayanhaote basins in northwestern China. In addition, the research results provide important geochemical parameters for reconstructing the dynamic evolution of the methane adsorption capacity of Jurassic shale gas reservoirs.

CRediT authorship contribution statement

Ruihui Zheng: Conceptualization, Writing – original draft, Resources. **Chengjin Zhang:** Supervision, Writing – review & editing. **Haizhong Tang:** Investigation, Data curation. **Zhihuan Zhang:** Writing – review & editing, Supervision, Funding acquisition. **Yuan Bao:** Writing – review & editing, Investigation. **Wenhao Li:** Writing – review & editing, Investigation. **Leyi Zhao:** Validation, Resources. **Tao Li:** Investigation, Resources. **Guangli Wang:** Investigation, Resources.

Declaration of competing interest

The authors declare that they have no known competing financial interests or personal relationships that could have appeared to influence the work reported in this paper.

Data availability

Data will be made available on request.

Acknowledgements

We sincerely thank Associate Editor Katz and other anonymous reviewers for their detailed and constructive comments that significantly improved the manuscript.

References

ASTM D7708-14, 2014. Standard Test Method for Microscopical Determination of the Reflectance of Vitrinite Dispersed in Sedimentary Rocks. ASTM, International, West Conshohocken, PA, USA, p. 10.

Barsotti, E., Tan, S.P., Saraji, S., Piri, M., Chen, J.H., 2016. A review on capillary condensation in nanoporous media: implications for hydrocarbon recovery from tight reservoirs. Fuel 184, 344–361.

Barrett, E.P., Joyner, L.G., Halenda, P.P., 1951. The determination of pore volume and area distributions in porous substances. I. Computations from nitrogen isotherms. J. Am. Chem. Soc. 73 (1), 378–380.

Bhargava, S., Awaja, F., Subasinghe, N.D., 2005. Characterisation of some Australian oil shale using thermal, X-ray and IR techniques. Fuel 184, 707–715.

Burnaz, L., Kalmykov, A., Grohmann, S., Kalmykov, G., Littke, R., 2022. Geochemistry and organic petrology of organic-rich shales of the upper jurassic – lower cretaceous bazhenov horizon in the frolov region, West Siberian basin: implications for the reconstruction of the organic matter origin and paleoredox conditions. Mar. Petrol. Geol. 143, 105809.

Brunauer, S., Deming, L.S., Deming, W.E., Teller, E., 1940. On a theory of the van der Waals adsorption of gases. J. Am. Chem. Soc. 62 (7), 1723–1732.

Brunauer, S., Emmett, P.H., Teller, E., 1938. Adsorption of gases in multimolecular layers. J. Am. Chem. Soc. 60 (2), 309–319.

Chalmers, G.R.L., Bustin, R.M., 2007. The organic matter distribution and methane capacity of the Lower Cretaceous strata of Northeastern British Columbia, Canada. Int. J. Coal Geol. 70 (1–3), 223–239.

Chen, G.H., Li, C., Lu, S.F., Guo, T.L., Wang, M., Xue, Q.Z., Zhang, T.Y., Li, Z.N., Sun, Y. H., Liu, J.Z., Jiang, S., 2021a. Critical factors controlling adsorption capacity of shale gas in Wufeng – Longmaxi formation, Sichuan Basin: evidences from both experiments and molecular simulations. J. Nat. Gas Sci. Eng. 88, 103774.

Chen, L., Jiang, Z.X., Liu, Q.X., Jiang, S., Liu, K.Y., Tan, J.Q., Gao, F.L., 2019. Mechanism of shale gas occurrence: insights from comparative study on pore structures of marine and lacustrine shales. Mar. Petrol. Geol. 104, 200–216.

Chen, J.H., Lan, H.X., Macciotta, R., Martin, C.D., Wu, Y.M., 2021b. Microfracture characterization of shale constrained by mineralogy and bedding. J. Petrol. Sci. Eng. 201, 108456.

Chen, J.P., Zhao, C.Y., Wang, Z.Y., He, Z.H., Qin, Y., 1998. Organic geochemical characteristics of oil, gas and source rocks of Jurassic coal measures in Northwestern China. Geol. Rev. 2, 149–159 (In Chinese with English abstract).

Cramer, B., Krooss, B.M., Littke, R., 1998. Modelling isotope fractionation during primary cracking of natural gas: a reaction kinetic approach. Chem. Geol. 149 (3–4), 235–250.

Curtis, J.B., 2002. Fractured shale-gas systems. AAPG (Am. Assoc. Pet. Geol.) Bull. 86 (11), 1921–1938.

Curtis, M.E., Cardott, B.J., Sondergeld, C.H., Rai, C.S., 2012. Development of organic porosity in the Woodford Shale with increasing thermal maturity. Int. J. Coal Geol. 103, 26–31.

Dai, J.X., Gong, D.Y., Ni, Y.Y., Huang, S.P., Wu, W., 2014. Stable carbon isotopes of coal-derived gases sourced from the Mesozoic coal measures in China. Org. Geochem. 74, 123–142.

Dang, W., Zhang, J.C., Tang, X., Wei, X.L., Li, Z.M., Wang, C.H., Chen, Q., Liu, C., 2018. Investigation of gas content of organic-rich shale: a case study from Lower Permian shale in southern North China Basin, central China. Geosci. Front. 9 (2), 559–575.

Dong, Y.G., 2014. Hydrocarbon Source Rocks Evaluation in Jurassic of Yabulai Basin of Inner Mangolia. China University of Geosciences, Beijing), pp. 89–92 (In Chinese with English abstract).

Fu, J.M., 1990. Geochemistry of Coal Formed Hydrocarbon. Science Press, Beijing, pp. 20–100.

Galimov, E.M., 1988. Sources and mechanisms of formation of gaseous hydrocarbons in sedimentary rocks. Chem. Geol. 71 (1/3), 77–95.

Gao, F.L., Song, Y., Jiang, Z.X., 2017. Influence of clay minerals on shale storage space and adsorptive capacity. Special Oil Gas Reservoirs 24 (3), 1–8 (In Chinese with English abstract).

Gao, J., Liu, G.D., Yang, W.W., Zhao, D.R., Chen, W., Liu, L., 2016. Geological and geochemical characterization of lacustrine shale, a case study of Lower Jurassic Badaowan shale in the Junggar Basin, Northwest China. J. Nat. Gas Sci. Eng. 31, 15–27.

Gao, Z.Y., Yang, S., Jiang, Z.X., Zhang, K., Chen, L., 2018. Investigating the spontaneous imbibition characteristics of continental Jurassic Ziliujing Formation shale from the northeastern Sichuan Basin and correlations to pore structure and composition. Mar. Petrol. Geol. 98, 697–705.

Gregg, S.J., Sing, K.S.W., 1982. Adsorption, Surface Area and Porosity. Academic Press, New York, p. 303.

Han, H., Pang, P., Zhong, N.N., Luo, Q.Y., Ma, Y., Gao, Y., 2020. The pore characteristics and gas potential of the Jurassic continental shales in the middle-small basins, northwest China. J. Petrol. Sci. Eng. 188, 106873.

Han, H., Zhong, N.N., Chen, C., Zhang, Y., Ma, Y., Wang, Q., 2014. The gas potential of Jurassic continental shale in the middle-small basins, Northwest China. Chin. Sci. Bull. 59 (9), 809–815 (In Chinese with English abstract).

He, Z.L., Nie, H.K., Zhao, J.H., Liu, W.X., Bao, F., Zhang, W.T., 2017. Types and origin of nanoscale pores and fractures in wufeng and Longmaxi shale in Sichuan Basin and its periphery. J. Nanosci. Nanotechnol. 17 (9), 6626–6633.
ISO1590-1, 2005. Pore Size Distribution and Porosity of Solid Materials by Mercury Porosimetry and Gas Adsorption-Part 1: Mercury Porosity. International Organization for Standardization, Geneva, Switzerland, p. 7.
ISO 7404-5, 2009. Methods for the Petrographic Analysis of Bituminous Coal and Anthracite-Part 5: Methods Determining Microscopically the Reflectance of Vitrinite. International Organization for Standardization, Geneva, Switzerland, p. 11.
Jarboe, P.J., Candela, P.A., Zhu, W.H., Kaufman, A.J., 2015. Extraction of hydrocarbons from high-maturity Marcellus shale using supercritical carbon dioxide. Energy Fuels 29, 7897–7909.
Jarvie, D.M., Hill, R.J., Ruble, T.E., Pollastro, R.M., 2007. Unconventional shale-gas systems: the Mississippiam Barnett Shale of north-central Texas as one model for thermogenic shale-gas assessment. AAPG (Am. Assoc. Pet. Geol.) Bull. 91, 475–499.
Jiang, Q.G., Wang, Q., Cheng, Q.Q., Zhang, C.M., Liu, W.B., 2005. Discussion on the kinetics characteristics of hydrocarbon generation of different maceral source rocks. Petroleum Geology & Experiment 27 (5), 512–533 (In Chinese with English abstract).
Ji, W.M., Song, Y., Jiang, Z.X., Wang, X.Z., Bai, Y.Q., Xing, J.Y., 2014. Geological controls and estimation algorithms of lacustrine shale gas adsorption capacity: a case study of the Triassic strata in the southeastern Ordos Basin, China. Int. J. Coal Geol. 134–135, 61–73.
Ji, W.M., Song, Y., Jiang, Z.X., Chen, L., Li, Z., Yang, X., Meng, M.M., 2015. Estimation of marine shale methane adsorption capacity based on experimental investigations of Lower Silurian Longmaxi formation in the Upper Yangtze Platform, south China. Mar. Petrol. Geol. 68, 94–106.
Kim, J., Kim, D., Lee, W., Lee, Y., Kim, H., 2017. Impact of total organic carbon and specific surface area on the adsorption capacity in Horn River shale. J. Petrol. Sci. Eng. 149, 331–339.
Ko, L.T., Loucks, R.G., Zhang, T., Ruppel, S.C., Shao, D., 2016. Pore and pore network evolution of Upper Cretaceous Boquillas (Eagle Ford-equivalent) mudrocks: results from gold-tube pyrolysis experiments. AAPG (Am. Assoc. Pet. Geol.) Bull. 100, 1693–1722.
Langmuir, I., 1918. The adsorption of gases on plane surfaces of glass, mica and platinum. J. Am. Chem. Soc. 40, 1361–1402.
Li, F.L., Wang, M.Z., Liu, S.B., Hao, Y.W., 2019. Pore characteristics and influencing factors of different types of shales. Mar. Petrol. Geol. 102, 391–401.
Li, Q.W., Liu, Z.B., Chen, F.R., Zhang, K., Tang, L., 2023. Behavior and controlling factors of methane adsorption in Jurassic continental shale, northeastern Sichuan Basin. Energy Geoscience 4, 83–92.
Li, T.W., Jiang, Z.X., Li, Z., Wang, P.F., Xu, C.L., Liu, G.H., Su, S.Y., Ning, C.X., 2017. Continental shale pore structure characteristics and their controlling factors: a case study from the lower third member of the Shahejie Formation, Zhanhua Sag, Eastern China. J. Nat. Gas Sci. Eng. 45, 670–693.
Li, X.B., Wan, Y.R., Wang, Q., Meng, Z.F., Lin, W.D., 2016. Characteristics of petroleum geology within middle and small basins and their resource potentials in Gansu and its adjacent regions. J. Lanzhou Univ. 42 (1), 18–22 (In Chinese with English abstract).
Li, X.Q., Horita, J., 2022. Kinetic and equilibrium reactions on natural and laboratory generation of thermogenic gases from Type II marine shale. Geochem. Cosmochim. Acta 333, 263–283.
Liu, B., Mohammadi, M., Ma, Z.L., Bai, L.H., Wang, L., Xu, Y.H., Hemmati-Sarapardeh, A., Ostadhassan, M., 2023. Pore structure evolution of Qingshankou shale (kerogen type I) during artificial maturation via hydrous and anhydrous pyrolysis: experimental study and intelligent modeling. Energy 282, 128359.
Liu, S.M., Tang, S.H., Tan, F.R., Zhao, C.L., Li, Y.H., Wang, S.J., Huo, T., 2020a. Pore structure characteristics and hydrocarbon generation potential of middle Jurassic lacustrine source rocks in the Yuka depression, Qaidam Basin, NW China: implications from petrographic and organic geochemical analyses. J. Nat. Gas Sci. Eng. 81, 103481.
Liu, S.M., Tang, S.H., Ma, C.Z., Yang, Y., Tan, F.R., Zhang, Y.X., Huo, T., 2020b. Geochemistry and reservoir characteristics of shale in the upper member of Shimengou Formation, Yuka sag. J. China Coal Soc. 45 (3), 1125–1136 (In Chinese with English abstract).
Liu, X.J., Xiong, J., Liang, L.X., 2015. Investigation of pore structure and fractal characteristics of organic-rich Yanchang formation shale in central China by nitrogen adsorption/desorption analysis. J. Nat. Gas Sci. Eng. 22, 62–72.
Loucks, R.G., Reed, R.M., Ruppel, S.C., Hammes, U., 2012. Spectrum of pore types and networks in mudrocks and a descriptive classification for matrix-related mudrock pores. AAPG (Am. Assoc. Pet. Geol.) Bull. 96 (6), 1071–1098.
Lu, S.F., Li, Z.D., Li, J.J., Liu, S.J., Huang, Z.K., Shen, J.H., Xue, H.T., 2009. Chemical kinetic method of evaluating low-mature gas and its application in Tuha Basin. Geochimica 38 (1), 68–74 (In Chinese with English abstract).
Luo, P., Ji, L.M., 2013. Reservoir characteristics and potential evaluation of continental shale gas. Nat. Gas Geosci. 24 (5), 1060–1068 (In Chinese with English abstract).
Ma, W.Y., Dilidaer, R.Z., Li, J., Liao, J.D., Wang, H.J., He, D., 2020. Hydrocarbon generation of Jurassic source rocks in the southern margin of Junggar Basin. Xinjing Pet. Geol. 41 (1), 31–37 (In Chinese with English abstract).
Ma, Y.X., Wang, Z.Y., Liang, M.J., Li, G.X., 2016. Cementing technology for Yabulai reservoir. West-China Explor. Eng. 28 (11), 54–55 (In Chinese with English abstract).
Miao, F., Wu, D., Liu, X.Y., Xiao, X.C., Zhai, W.B., Geng, Y.Y., 2022. Methane adsorption on shale under in situ conditions: gas-in-place estimation considering in situ stress. Fuel 308, 121991.
Milliken, K.L., Rudnicki, M., Awwiller, D.N., Zhang, T.W., 2013. Organic matter-hosted pore system, Marcellus Formation (devonian), Pennsylvania. AAPG (Am. Assoc. Pet. Geol.) Bull. 97 (2), 177–200.
Montgomery, S.L., Jarvie, D.M., Bowker, K.A., Pollastro, R.M., 2005. Mississippian Barnett Shale, Fort Worth basin, north-central Texas: gas-shale play with multi-trillion cubic foot potential. AAPG (Am. Assoc. Pet. Geol.) Bull. 89 (2), 155–175.
Ni, Y.Y., Zhang, D.J., Liao, F.R., Gong, D.Y., Xue, P., Yu, F., Yu, J.Z., Chen, J.P., Zhao, C.Y., Hu, J., Jin, Y., 2015. Stable hydrogen and carbon isotopic ratios of coal-derived gases from the Turpan-Hami Basin, NW China. Int. J. Coal Geol. 152, 144–155.
Passey, Q.R., Bohacs, K.M., Esch, W.L., Sinha, S., 2010. From oil-prone source rock to gas-producing shale reservoir-geologic and petrophysical characterization of unconventional shale-gas reservoirs. In: CPS/SPE International Oil & Gas Conference and Exhibition in China.
Qian, Y., Wang, Z.D., Zhang, T., Tuo, J.C., Wang, X.F., Wang, Z.Y., Xu, Y.C., 2017. Geochemical characteristics of Jurassic source rocks and natural gas in the eastern Junggar Basin and exploration potential pf low-mature gas. Acta Pet. Sin. 38 (1), 44–54 (In Chinese with English abstract).
Ross, D.J.K., Bustin, R.M., 2008. Characterizing the shale gas resource potential of Devonian-Mississippian strata in the Western Canada sedimentary basin: application of an integrated formation evaluation. AAPG (Am. Assoc. Pet. Geol.) Bull. 92 (1), 87–125.
Ross, D.J.K., Bustin, R.M., 2009. The importance of shale composition and pore structure upon gas storage potential of shale gas reservoirs. Mar. Petrol. Geol. 26 (6), 916–927.
Rouquerol, J., Avnir, D., Fairbridge, C.W., Everett, D.H., Haynes, J.H., Pernicone, N., Ramsay, J.D.F., Sing, K.S.W., Unger, K.K., 1994. Recommendations for the characterization of porous solids. Pure Appl. Chem. 66 (8), 1739–1758.
Schaefer, R.G., Galushkin, Y.L., Kolloff, A., Littke, R., 1999. Reaction kinetics of gas generation in selected source rocks of the West Siberian Basin: implications for the mass balance of early-thermogenic methane. Chem. Geol. 156 (1–4), 41–65.
Shao, L.Y., Li, M., Li, Y.H., Zhang, Y.P., Lu, J., Zhang, W.L., Tian, Z., Wen, H.J., 2014. Geological characteristics and controlling factors of shale gas in the Jurassic of the northern Qaidam Basin. Earth Sci. Front. 21 (4), 311–322 (In Chinese with English abstract).
Shao, L.Y., Liu, L., Wen, H.J., Li, Y.H., Zhang, W.L., Li, M., 2016. Characteristics and influencing factors of nanopores in the Middle Jurassic Shimengou shale in well YQ-1 of the northern Qaidam Basin. Earth Sci. Front. 23 (1), 164–173 (In Chinese with English abstract).
Sing, K.S.W., 1982. Reporting physisorption data for gas/solid systems with special reference to the determination of surface area and porosity. Pure Appl. Chem. 54 (11), 2201–2218.
Sun, X.G., Wang, G.Y., Jin, K.L., 1999. The kinetic features of hydrocarbon generation of desmocollinite. Chinses Journal of Geology (Scientia Geologica Sinica) 34 (1), 485–491 (In Chinese with English abstract).
Tian, T., Ren, Z.L., Wu, X.Q., Ma, G.F., Zhang, R.S., Yang, Z.M., Guo, K., 2015. The paleogeothermal field and hydrocarbon accumulation period in Sartai depression, Yabulai Basin. Acta Sedimentol. Sin. 33 (4), 836–844 (In Chinese with English abstract).
Tian, T., 2015. Study on the Thermal History and Hydrocarbon Accumulation Periods of Saertai Depression in the Yabulai Basin. Northwest University (Xi'an), pp. 97–101 (In Chinese with English abstract).
Wang, D.D., Shao, L.Y., Li, Z.X., Li, M.P., Lv, D.W., Liu, H.Y., 2016. Hydrocarbon generation characteristics, reserving performance and preservation conditions of continental coal measure shale gas: a case study of Mid-Jurassic shale gas in the Yan'an Formation, Ordos Basin. J. Petrol. Sci. Eng. 145, 609–628.
Wang, F.L., Feng, Z.H., Wang, X., Zeng, H.S., 2023a. Effect of organic matter, thermal maturity and clay minerals on pore formation and evolution in the Gulong Shale, Songliao Basin, China. Geoenergy Science and Engineering 223, 211507.
Wang, N.Z., Guo, T.L., Li, M.W., Xiong, L., Dong, X.X., Wang, T., Ouyang, J.S., 2023b. Reservoir characteristics and oil properties of a lacustrine shale system: early Jurassic black shale from the Sichuan Basin, SW China. J. Asian Earth Sci. 242, 105491.
Wang, S.B., Song, Z.G., Cao, T.T., Song, X., 2013. The methane sorption capacity of Paleozoic shales from the Sichuan Basin, China. Mar. Petrol. Geol. 44, 112–119.
Wang, X.F., Xu, Y.C., Shen, P., Zheng, J.J., Shi, B.G., 2010. Geochemical characteristics and identification indexes of low-mature gases. Nat. Gas Geosci. 21 (1), 1–6 (In Chinese with English abstract).
Wang, X., Wang, M., Li, J.B., Shao, H.M., Deng, Z.X., Wu, Y., 2022. Thermal maturity: the controlling factor of wettability, pore structure, and oil content in the lacustrine Qingshankou shale, Songliao Basin. J. Petrol. Sci. Eng. 215, 110618.
Wang, Y.B., 2014. Analysis on Geochemical Characteristics and Potentials of Xinhe Formation in Yabulai Basin. Xi'an Shiyou University (Xi'an), pp. 10–27 (In Chinese with English abstract).
Washburn, E.W., 1921. Note on the Method of Determining the Distribution of Pore Sizes in a Porous Material.
Wu, C.J., Zhang, M.F., Xiong, D.M., Tuo, J.C., Ma, W.Y., Qian, Y., 2020. Gas generation from Jurassic coal measures at low mature stage and potential gas accumulation in the eastern Junggar Basin, China. J. Nat. Gas Sci. Eng. 84, 103692.
Wu, M.B., Liu, C.Y., Zheng, M.L., Yun, J.B., 2007. Jurassic depositional – tectonic evolution in the Yabulai basin, western Inner Mongolia, China and direction of petroleum exploration. Geol. Bull. China 26 (7), 857–863 (In Chinese with English abstract).
Wu, X.Z., Wang, G.J., Zheng, M., Zheng, M., 2015. Structural evolution and hydrocarbon accumulation in Yabulai Basin. Chinese Journal of Geology (Scientia Geologica Sinica) 50 (1), 74–87 (In Chinese with English abstract).
Xing, J.Y., Hu, S.B., Jiang, Z.X., Wang, X.Z., Wang, J.L., Sun, L., Bai, Y.F., Chen, L., 2018. Classification of controlling factors and determination of a prediction model for

shale gas adsorption capacity: a case study of Chang 7 shale in the Ordos Basin. J. Nat. Gas Sci. Eng. 49, 260–274.
Xu, J., Zhang, C.M., Xie, X.M., Rui, X.Q., 2018. Separation of macerals in organic-rich source rocks and their geochemical characteristics. Petroleum Geology & Experiment 40 (6), 828–835 (In Chinese with English abstract).
Xu, Y.C., Wang, X.F., Shi, B.G., 2009. Low mature gas: an extension of the concept of coal-formed gas. Petrol. Explor. Dev. 36, 408–412.
Ye, Y.P., Tang, S.H., Xi, Z.D., Jiang, D.X., Duan, Y., 2022. Quartz types in the Wufeng-Longmaxi Formations in southern China: implications for porosity evolution and shale brittleness. Mar. Petrol. Geol. 137, 105479.
Zhang, P.F., Lu, S.F., Li, J.Q., Xue, H.T., Li, W.H., Zhang, P., 2017. Characterization of shale pore system: a case study of Paleogene Xin'gouzui Formation in the Jianghan basin, China. Mar. Petrol. Geol. 79, 321–334.
Zhang, S.M., Cao, Y.C., Jens, J., Zhu, R.K., Mao, Z.G., Xi, L.L., Kashif, M., Helge, H., 2018. Pore characteristics of the fine-grained tight reservoirs in the Yabulai Basin, northestern China. Acta Geol. Sin. 92 (3), 1170–1192.
Zhang, T.W., Ellis, G.S., Ruppel, S., Milliken, K., Yang, R.S., 2012. Effect of organic-matter type and thermal maturity on methane adsorption in shale-gas systems. Org. Geochem. 47, 120–131.
Zhang, Y.P., Li, Y.H., Guo, W., Han, W., Li, Y.H., Wang, W.C., 2021. Characteristics and main controlling factors of pore structures in low thermal maturity continental shale of Jurassic, northern Qaidam basin. Acta Geol. Sin. 95 (2), 565–577 (In Chinese with English abstract).
Zhao, W.Z., Li, J.Z., Yang, T., Wang, S.F., Huang, J.L., 2016. Geological difference and its significance of marine shale gases in South China. Petrol. Explor. Dev. 43 (4), 499–510.
Zhao, W.Z., Zhang, Y., Zhao, C.Y., Xu, D.F., 1996. Formation and distribution of coal measure-derived hydrocarbon accumulation in NW China. Acta Pet. Sin. 17 (2), 1–8 (In Chinese with English abstract).
Zheng, R.H., Wang, Y.F., Li, Z.P., Zhang, Z.H., Wang, G.L., Zhang, H., 2022. Differences and origins of hydrocarbon generation characteristics between mudstone and shale in the seventh member of the Yanchang Formation, Ordos Basin, China. Int. J. Coal Geol. 257, 104012.
Zou, C.N., Dong, D.Z., Wang, S.J., Li, J.Z., Li, X.J., Wang, Y.M., Li, D.H., Cheng, K.M., 2010. Geological characteristics, formation mechanism and resource potential of shale gas in China. Petrol. Explor. Dev. 37 (6), 641–653 (In Chinese with English abstract).